

On the bipolarity of Wolf-Rayet nebulae

D. M.-A. Meyer*

Universität Potsdam, Institut für Physik und Astronomie, Karl-Liebknecht-Strasse 24/25, 14476 Potsdam, Germany

Received; accepted

ABSTRACT

Wolf-Rayet stars are amongst the rarest but also most intriguing massive stars. Their extreme stellar winds induce famous multi-wavelength circumstellar gas nebulae of various morphologies, spanning from circles and rings to bipolar shapes. This study is devoted to the investigation of the formation of young, asymmetric Wolf-Rayet gas nebulae and we present a 2.5-dimensional magneto-hydrodynamical toy model for the simulation of Wolf-Rayet gas nebulae generated by wind-wind interaction. Our method accounts for stellar wind asymmetries, rotation, magnetisation, evolution and mixing of materials. It is found that the morphology of the Wolf-Rayet nebulae of blue supergiant ancestors is tightly related to the wind geometry and to the stellar phase transition time interval, generating either a broadened peanut-like or a collimated jet-like gas nebula. Radiative transfer calculations of our Wolf-Rayet nebulae for dust infrared emission at $24\ \mu\text{m}$ show that the projected diffuse emission can appear as oblate, bipolar, ellipsoidal or ring structures. Important projection effects are at work in shaping observed Wolf-Rayet nebulae. This might call a revision of the various classifications of Wolf-Rayet shells, which are mostly based on their observed shape. Particularly, our models question the possibility of producing pre-Wolf-Rayet wind asymmetries, responsible for bipolar nebulae like NGC 6888, within the single red supergiant evolution channel scenario. We propose that bipolar Wolf-Rayet nebulae can only be formed within the red supergiant scenario by multiple/merged massive stellar systems, or by single high-mass stars undergoing additional, e.g. blue supergiant, evolutionary stages prior to the Wolf-Rayet phase.

Key words: methods: MHD – radiative transfer – stars: massive – stars: circumstellar matter.

1 INTRODUCTION

Formed out of the gravitational collapse of opaque pre-stellar cores, high-mass stellar objects, i.e. with mass $\geq 8 M_{\odot}$, are cosmic regulators of the cycle of matter at work in the interstellar medium (ISM) of galaxies (Maeder 2009; Langer 2012). One of their characteristic features is the fast and strong wind blown out from their surface and powered by the complex nuclear reactions at work in their interior. Throughout their lives, massive stars first experience a rather long, main-sequence phase corresponding to the burning of hydrogen in their cores (Ekström et al. 2012). It is characterised by the release of diluted, hot and supersonic winds from the stellar surface, and, once their hydrogen is exhausted, stellar evolution is triggered. The entire evolution of massive stars is fixed by their zero-age main-sequence properties, such as their mass, angular velocity and chemical composition, which uniquely determines their evolution and ultimate fate (Woosley et al. 2002; Vink 2006; Brott et al. 2011; Szécsi et al. 2020). These initial stellar characteristics rule the time-dependence of the stellar surface properties, as well as the number and duration of the various evolutionary

phases, up to their death, either as a core-collapse supernova leaving behind a plerionic supernova remnant, or directly collapsing as a black hole (Chevalier 1977; Weiler & Sramek 1988; Woosley et al. 2002; Woosley & Bloom 2006; Smartt 2009; Müller & Janka 2015; Gabler et al. 2021).

Amongst the many possible evolutionary histories massive stars can undergo, high-mass stellar objects can evolve to the so-called Wolf-Rayet stage. This phase is characterised by fast ($\sim 1000\text{--}5000\ \text{km s}^{-1}$) and dense stellar winds expelled at mass-loss rates $\geq 10^{-5} M_{\odot} \text{ yr}^{-1}$ and enriched in C, N and O elements (Hamann et al. 2006; Sander et al. 2012; Bestenlehner et al. 2014). The precise manner a massive stellar object acquires the spectroscopic properties of a Wolf-Rayet star is not completely understood, however, a few typical evolutionary paths have been identified (Crowther 2007). The most common channel reposes in an evolution from the main-sequence to the Wolf-Rayet phase through a red supergiant phase, and it mostly concerns Galactic stars with masses $\geq 20 M_{\odot}$. Heavier zero-age main-sequence stars (up to $\sim 60 M_{\odot}$) have been shown theoretically to experience a much more complex evolution, including several successive luminous blue variable phases, during which the star blows, sometimes eruptively, blue supergiant material (Groh et al. 2014).

The interaction of the stellar wind of massive stars with the

* E-mail: dmameyer.astro@gmail.com

ISM produces gas nebulae witnessing the release of energy, momentum and heavy chemical elements which enriched their local ambient medium (Langer 2012). The classical picture for stellar wind-ISM interaction is that of Weaver et al. (1977) and it consists of a several parsec-scale structured circumstellar bubbles surrounding massive stars. The circumstellar medium of Wolf-Rayet stars is different, as many of them display unusual smaller-scale ring-like gas nebulae detected in H α and infrared, both in the Milky Way, see Chu & Treffers (1981) and Treffers & Chu (1982), and in the Magellanic Clouds (Chu 1982b, 1983; Dopita et al. 1994; Weis et al. 1997; Hung et al. 2021), respectively. A classification of circumstellar structures around Wolf-Rayet stars arose from that studies (Chu 1981, 1982b,a; Treffers & Chu 1982; Chu et al. 1983; Toalá et al. 2015). Several follow-up surveys deepened and completed these observations in the southern hemisphere, see Marston et al. (1994) and Marston et al. (1994). Wolf-Rayet nebulae entered the X-rays domain with *Asca* (Wrigge et al. 2005) *Rosat* and *Chandra* (Guerrero & Chu 2008), *XMM-Newton* (Toalá et al. 2012) observations from their (shocked) stellar winds witnessing emission of optically-thin high temperature plasma. More recently, a radio non-thermal synchrotron counterpart of the stellar wind bubble of a Wolf-Rayet ring nebula indicated that these circumstellar nebulae are the site of particles acceleration (Prajapati et al. 2019). This accumulation of observations motivates the present numerical efforts aiming at understanding the peculiar vicinity of young Wolf-Rayet stars.

Numerical simulations rapidly became an efficient tool to understand the different physical processes at work in the circumstellar medium of massive stars (Comerón & Kaper 1998; Freyer et al. 2003; Dwarkadas 2005; Freyer et al. 2006; Toalá & Arthur 2011; van Marle et al. 2011, 2015), to constrain stellar evolution models/probe local ISM conditions (Mackey et al. 2012, 2014), and to understand the pre-supernova surroundings of dying massive stars, with which supernovae shock waves subsequently interact (Ciotti & D’Ercole 1989; Chevalier & Liang 1989; van Marle et al. 2005, 2006; Meyer et al. 2021). Particularly, the gas nebulae formed around Wolf-Rayet stars have been studied numerically as evolved winds, colliding with the material of a larger-scale main-sequence wind-blown bubble (Brighenti & D’Ercole 1997; Dwarkadas 2007; van Marle et al. 2007, 2011).

It has recently been shown in Meyer et al. (2020), on the basis of magneto-hydrodynamical (MHD) simulations, that (i) the circumstellar rings appearing to be comoving with the fastest-moving Wolf-Rayet stars are a trace of their very high initial masses (≥ 35 to $\sim 60 M_{\odot}$) inducing complex evolutionary histories, and that (ii) their large-scale surroundings are main-sequence stellar wind bow shocks fainter than the inner rings which became unobservable as the driving star runs into diluted media (Gvaramadze et al. 2010). This solved the apparent missing bow shock problem around some high-latitude, Galactic, very fast-moving Wolf-Rayet stars like WR124, surrounded by its compact gas nebula M1-67 (Chu 1981; van der Sluys & Lamers 2003; Marchenko et al. 2010; Toalá et al. 2018) or WR71 (Faherty et al. 2014; Flagey et al. 2014). If we can now qualitatively explain the formation of quasi-spherical rings around very fast-moving Wolf-Rayet stars, detailed observations of these gas nebulae reveal much more complex structures whose formation are far from being understood. Which mechanisms distinguish between the production of ring-like shells from ovoidal and/or other complex shapes? What can we learn regarding the past evolution of massive stars with nebulae of such morphologies?

In this study, we continue our investigations of the shaping

of circumstellar Wolf-Rayet nebulae started in Meyer et al. (2020). We concentrate on the production of bipolar asymmetries and non-spherical morphologies observed in the vicinity of some young Wolf-Rayet stars (Toalá et al. 2015). The starting point of this study is the work of Brighenti & D’Ercole (1997), in which the development of young aspherical Wolf-Rayet nebulae is examined using an hydrodynamical wind-wind interaction model. Their simulations focus on the particular scenario of a red supergiant star, with asymmetric stellar wind properties, evolving to a Wolf-Rayet stage of symmetric stellar wind properties. In the same spirit, we build a magneto-hydrodynamical toy model for rotating blue supergiant stars with asymmetric stellar winds and evolving to the Wolf-Rayet phase. The effects of asymmetries in the blue supergiant wind are investigated using the recipe of Raga et al. (2008). We perform near-infrared synthetic observables of the corresponding bipolar stellar wind nebulae, in order to discuss their respective emission properties and facilitate qualitative comparison to observations available in the literature.

Our study is organised as follows. Firstly, we present the numerical methods utilised for the MHD simulations of Wolf-Rayet gas nebulae evolving after having undergone a previous blue supergiant phase in Section 2. We show our results regarding to the dynamical evolution of bipolar MHD Wolf-Rayet nebulae generated by wind-wind interaction in Section 3. The results are further discussed in Section 4, and finally, we present our conclusions in Section 5.

2 METHOD

This section presents the numerical methods used in this project, together with the initial conditions and parametrised boundary conditions of the simulations. Last, we introduce the reader to the models performed in this study.

2.1 Governing equations

We set our problem in the frame of non-ideal magneto-hydrodynamics, described by the following series of equations,

$$\frac{\partial \rho}{\partial t} + \nabla \cdot (\rho \mathbf{v}) = 0, \quad (1)$$

$$\frac{\partial \mathbf{m}}{\partial t} + \nabla \cdot (\mathbf{m} \otimes \mathbf{v} - \mathbf{B} \otimes \mathbf{B} + \hat{\mathbf{I}} p_t) = \mathbf{0}, \quad (2)$$

$$\frac{\partial E}{\partial t} + \nabla \cdot ((E + p_t) \mathbf{v} - \mathbf{B} (\mathbf{v} \cdot \mathbf{B})) = \Phi(T, \rho), \quad (3)$$

and,

$$\frac{\partial \mathbf{B}}{\partial t} + \nabla \cdot (\mathbf{v} \otimes \mathbf{B} - \mathbf{B} \otimes \mathbf{v}) = \mathbf{0}, \quad (4)$$

where \mathbf{B} represents the magnetic field vector, ρ stands for the mass density,

$$\mathbf{m} = \rho \mathbf{v}, \quad (5)$$

is the linear momentum vector, $\hat{\mathbf{I}}$ the identity matrix, p_t is the total pressure and \mathbf{v} the gas velocity, respectively. The total energy of the system reads,

$$E = \frac{p}{(\gamma - 1)} + \frac{\mathbf{m} \cdot \mathbf{m}}{2\rho} + \frac{\mathbf{B} \cdot \mathbf{B}}{2}, \quad (6)$$

Table 1. Stellar surface parameters used in our two-winds models.

Quantities	Symbol	Supergiant	Wolf-Rayet
Accretion rate	\dot{M} ($M_{\odot} \text{ yr}^{-1}$)	10^{-6}	$10^{-4.3}$
Wind velocity	v_w (km s^{-1})	500	1900
Angular velocity	v_{rot} (km s^{-1})	60	10
Surface field	B_{\star} (G)	1	100
Stellar radius	R_{\star} (R_{\odot})	20	2.3

and the sound speed is defined as,

$$c_s = \sqrt{\frac{\gamma p}{\rho}}, \quad (7)$$

which closes the above system of equations, and where $\gamma = 5/3$ is the adiabatic index.

Radiative cooling and heating of the gas,

$$\Phi(T, \rho) = n_{\text{H}}\Gamma(T) - n_{\text{H}}^2\Lambda(T), \quad (8)$$

are explicitly included via optically-thin processes for loss $\Lambda(T)$ and gain $\Gamma(T)$ in the the source term, where,

$$T = \mu \frac{m_{\text{H}} p}{k_{\text{B}} \rho}, \quad (9)$$

is the gas temperature, and using the laws of photoionized gas described in great detail in Meyer et al. (2021). Hence, our method ignores any explicit treatment of the radiation pressure from the photon field of the central star. This is correct for cool blue supergiant stars, while we neglect the detailed position of the ionization front generated by the young Wolf-Rayet stars, as well as its effects on the shell instabilities (Toalá & Arthur 2011).

A passive scalar tracer is included in the stellar wind,

$$\frac{\partial(\rho Q)}{\partial t} + \nabla \cdot (v\rho Q) = 0, \quad (10)$$

to follow the advection of the new-born Wolf-Rayet circumstellar nebula, as compared to the previous blue supergiant wind. This system of equations is solved by use of the eight-wave algorithm (Powell 1997), within a second-order Runge-Kutta with parabolic reconstruction of the variables between neighbouring cells together with the HLL Riemann solver (Harten et al. 1983). This unsplit scheme ensures that the magnetic field is divergence-free everywhere in the computational domain. The simulations timesteps are controlled by the Courant-Friedrich-Levi condition that we set to $C_{\text{cfl}} = 0.1$.

2.2 Initial conditions

We carry out MHD simulations with the PLUTO code (Mignone et al. 2007, 2012; Vaidya et al. 2018). The calculations are performed using a 2.5-dimensional spherical coordinate system ($O;r,\theta,\phi$) of origin O , with r the radial direction, θ the poloidal coordinate and ϕ the toroidal component. The coordinate system $[r_{\text{in}}, r_{\text{out}}] \times [0, \pi] \times [0, 2\pi]$ is mapped with a mesh that is uniform along the polar and toroidal directions, while it expands logarithmically along the radial direction. It permits to reach high spatial resolutions close to the stellar wind boundary $r_{\text{in}} = 0.02$ pc, while reducing the total number of grid zones in the simulation domain and reducing the computational costs. In total, we use $200 \times 200 \times 1$ grid zones. Outflow boundary conditions are assigned at the outer boundary $r_{\text{out}} = 10$ pc, reflective boundary conditions are imposed along the symmetry axis $\theta = 0$ and $\theta = \pi$, while periodic boundary conditions are used at the borders $\phi = 0$ and $\phi = 2\pi$.

Since the inner boundary is much larger than the radius of the photosphere ($r_{\text{in}} \gg R_{\star}$), stellar gravity and wind acceleration mechanisms such as coronal heating and radiation pressure, are neglected in the computational domain. Therefore, the acceleration of the stellar wind to the terminal velocity is not modelled in the simulations.

The simulations are initialised with the asymmetric stellar wind of a blue supergiant star. The adopted latitude-dependence of the wind density is that developed in the context of the astrosphere of the runaway asymptotic giant branch star Mira (Raga et al. 2008). It reads,

$$\rho_w(r, \theta) = \frac{\dot{M}}{4\pi r^2 v_w} \rightarrow \frac{A}{r^2} f(\theta), \quad (11)$$

with \dot{M} the stellar mass-loss rate, v_w the stellar wind velocity and r the radial distance to the central star. The function,

$$f(\theta) = \xi - (\xi - 1)|\cos(\theta)|^p, \quad (12)$$

measures the wind anisotropy, with p a parameter determining the flattening degree of the density towards the equator and ξ is the equator-to-pole density ratio, respectively. The scaling factor A ensures that the latitude-dependence in the stellar wind conserves the amount of mass lost by the star per unit time. It is evaluated by writing the mass conservation at the stellar surface,

$$\dot{M} = 4\pi r^2 \int_0^{\pi/2} \rho_w(r, \theta) v_w(r, \theta) \sin(\theta) d\theta, \quad (13)$$

yielding,

$$\dot{M} = 4\pi A v_w \int_0^{\pi/2} |f(\theta)|^p \sin(\theta) d\theta, \quad (14)$$

where v_w is the stellar wind terminal velocity, and, finally, one obtains,

$$A = \frac{\dot{M}}{4\pi v_w} \frac{(\xi - 1)^2}{8\xi^{5/2} - 20\xi + 12}, \quad (15)$$

using $p = 1/2$. We chose this prescriptions for stellar wind asymmetries since it has already been used in the context of massive stars (Fang et al. 2017), although other recipes exist (Frank et al. 1995; Blondin et al. 1996).

Additionally, Raga et al. (2008) prescribe stellar wind flow assigned at the wind boundary r_{in} to account for the asymmetry function as,

$$v(r_{\text{in}}, \theta) = \frac{v_w}{\sqrt{f(\theta)}}, \quad (16)$$

so that the ram pressure of the wind of the inner boundary,

$$\rho_w(r_{\text{in}}, \theta) v(r_{\text{in}}, \theta)^2 = \frac{A}{r_{\text{in}}^2} f(\theta) \left(\frac{v_w}{\sqrt{f(\theta)}} \right)^2 \propto \left(\frac{v_w}{r_{\text{in}}} \right)^2, \quad (17)$$

remains isotropic. Stellar rotation is included in the model by considering the following latitude-dependent equatorial rotation velocity,

$$v_{\phi}(\theta) = v_{\text{rot}} \sin(\theta), \quad (18)$$

where v_{rot} is the star's equatorial rotation speed. Last, the magnetisation of the stellar winds is treated as a Parker spiral. It is a split monopole,

$$B_r(r) = B_{\star} \left(\frac{R_{\star}}{r} \right)^2, \quad (19)$$

where R_{\star} is the stellar radius, B_{\star} the stellar surface magnetic field,

Table 2. List of models in our study. The table informs on the simulation labels, whether the blue supergiant wind is symmetric or not, the blue supergiant to Wolf-Rayet phase transition timescale Δt (in yr) and the exponent β controlling the variations of the different quantities during the phase transition, the flattening degree of the blue supergiant wind towards the equator p and the equator-to-pole density ratio ξ , respectively. The last column gives the general purpose of each simulation models.

Model	Asymmetric wind	Δt (yr)	β	p	ξ	Purpose
Run-Base	yes	0	4	1/4	20	Baseline model
Run-Sym	no	0	—	—	—	Model with isotropic progenitor wind
Run- Δt 10kyr	yes	10^4	4	1/4	20	Model with Δt 10kyr phase transition
Run- ξ 20	yes	10^4	4	1/4	20	Model with phase transition and lower pole-to-equator density contrast
Run- ξ 100	yes	10^4	4	3/4	100	Model with phase transition and higher pole-to-equator density contrast
Run- β 4	yes	5×10^4	4	1/4	20	Model with quadratic interpolation between winds during the phase transition
Run- β 2	yes	5×10^4	4	1/4	20	Model with linear interpolation between winds during the phase transition

plus a toroidal component,

$$B_\phi(r) = B_r(r) \left(\frac{v_\phi(\theta)}{v_w} \right) \left(\frac{r}{R_\star} - 1 \right), \quad (20)$$

which relies on both the stellar surface magnetic field strength and on the stellar rotation velocity v_{rot} . This so-called Parker stellar wind is a parametrisation for magnetised low-mass stars which has been developed and widely-used in studies devoted to the heliosphere (Parker 1958; Pogorelov & Semenov 1997; Pogorelov & Matsuda 2000; Pogorelov et al. 2004). It has been adapted to the intermediate stellar mass regime in works investigating the shaping of planetary nebula (Chevalier & Luo 1994; Rozyczka & Franco 1996; García-Segura et al. 2018, 2020) and stellar wind bow shocks (Herbst et al. 2020; Scherer et al. 2020; Meyer et al. 2021), respectively.

2.3 Time-dependent stellar boundary conditions

At time $t_{\text{wr}} - \Delta t$ the blue supergiant to Wolf-Rayet phase begins to take place, controlled by several quantities, namely its duration Δt and the manner the surface stellar properties evolve, determined by the quintuplet $(\dot{M}, v_w, v_{\text{rot}}, B_\star, R_\star)$. The stellar wind velocity is modulated following (Brighenti & D’Ercole 1997),

$$v_w(r_{\text{in}}, t) = \begin{cases} v_w^{\text{bsg}} / \sqrt{f(\theta)} & \text{if } t \leq t_{\text{wr}} - \Delta t, \\ v_w^{\text{bsg}} / \sqrt{f(\theta)} + \Delta v F & \text{if } t_{\text{wr}} - \Delta t < t \leq t_{\text{wr}}, \\ v_w^{\text{wr}} & \text{if } t_{\text{wr}} < t, \end{cases} \quad (21)$$

with $\Delta v = |v_w^{\text{wr}} - v_w^{\text{bsg}}|$. In the above and following relations, the superscript “bsg” and “wr” stand for the blue supergiant and Wolf-Rayet winds, respectively. The manner the wind velocity changes over Δt is controlled by,

$$F = F(t, t_{\text{wr}}, \Delta t) = \left(\frac{t - (t_{\text{wr}} - \Delta t)}{\Delta t} \right)^{\beta/2}, \quad (22)$$

that is a function invoked when $t_{\text{wr}} - \Delta t < t$ and $t \leq t_{\text{wr}}$, defined such that $F(t = t_{\text{wr}} - \Delta t) = 0$ and $F(t = t_{\text{wr}}) = 1$. For $\beta = 2$ the transition is linear, while it is a power-law for $\beta \neq 2$. The changes in wind density are as follows,

$$\dot{M}(r_{\text{in}}, t) = \begin{cases} \dot{M}^{\text{bsg}} & \text{if } t \leq t_{\text{wr}}, \\ \dot{M}^{\text{wr}} & \text{if } t_{\text{wr}} < t, \end{cases} \quad (23)$$

with a sharp transition at t_{wr} (Brighenti & D’Ercole 1997). These relations implies that only the Wolf-Rayet wind is launched isotropically while the previous winds are affected by the isotropy function $f(\theta)$.

Our MHD setup requires additional, similar prescriptions for the other quantities necessary to fully fix both the Parker spiral and the passive tracers tracking the mixing of material into the gas nebula. We introduce, in the same fashion as done for the hydrodynamical case of Brighenti & D’Ercole (1997), prescriptions for the toroidal and poloidal components of the stellar surface magnetic field. They read,

$$R_\star(r_{\text{in}}, t) = \begin{cases} B_\star^{\text{bsg}} & \text{if } t \leq t_{\text{wr}} - \Delta t, \\ B_\star^{\text{bsg}} + \Delta B_\star F & \text{if } t_{\text{wr}} - \Delta t < t \leq t_{\text{wr}}, \\ B_\star^{\text{wr}} & \text{if } t_{\text{wr}} < t, \end{cases} \quad (24)$$

with $\Delta B_\star = |B_\star^{\text{wr}} - B_\star^{\text{bsg}}|$. Equivalently, the stellar radius evolves as,

$$R_\star(r_{\text{in}}, t) = \begin{cases} R_\star^{\text{bsg}} & \text{if } t \leq t_{\text{wr}} - \Delta t, \\ \Delta R_\star (1 - F) + R_\star^{\text{wr}} & \text{if } t_{\text{wr}} - \Delta t < t \leq t_{\text{wr}}, \\ R_\star^{\text{wr}} & \text{if } t_{\text{wr}} < t, \end{cases} \quad (25)$$

with $\Delta R_\star = |R_\star^{\text{bsg}} - R_\star^{\text{wr}}|$. Finally, the time-dependent evolution of the equatorial angular velocity reads,

$$v_{\text{rot}}(r_{\text{in}}, t) = \begin{cases} v_{\text{rot}}^{\text{bsg}} & \text{if } t \leq t_{\text{wr}} - \Delta t, \\ \Delta v_{\text{rot}} (1 - F) + v_{\text{rot}}^{\text{wr}} & \text{if } t_{\text{wr}} - \Delta t < t \leq t_{\text{wr}}, \\ v_{\text{rot}}^{\text{wr}} & \text{if } t_{\text{wr}} < t, \end{cases} \quad (26)$$

with $\Delta v_{\text{rot}} = |v_{\text{rot}}^{\text{bsg}} - v_{\text{rot}}^{\text{wr}}|$. Last, the evolution of the passive scalar tracer at the stellar wind boundary obeys the relation,

$$Q(r_{\text{in}}, t) = \begin{cases} 0 & \text{if } t \leq t_{\text{wr}} - \Delta t, \\ F & \text{if } t_{\text{wr}} - \Delta t < t \leq t_{\text{wr}}, \\ 1 & \text{if } t_{\text{wr}} < t, \end{cases} \quad (27)$$

which permits to separate the cold, dusty, blue supergiant gas ($Q \leq 1/2$) from the Wolf-Rayet material ($Q > 1/2$).

2.4 Simulation models

The simulations are initialised with stellar wind properties corresponding to a blue supergiant star. We let the system evolved to a few 10^4 yr up to a time $t_{\text{wr}} - \Delta t$. This time interval corresponds to the typical timescale of a luminous blue variable phase (Smith 2017) and it permits to have potential magneto-hydrodynamical boundary effects provoked by the onset of stellar rotation at $t = 0$ to be transported out of the computational domain under the effects of the constant wind inflow. The

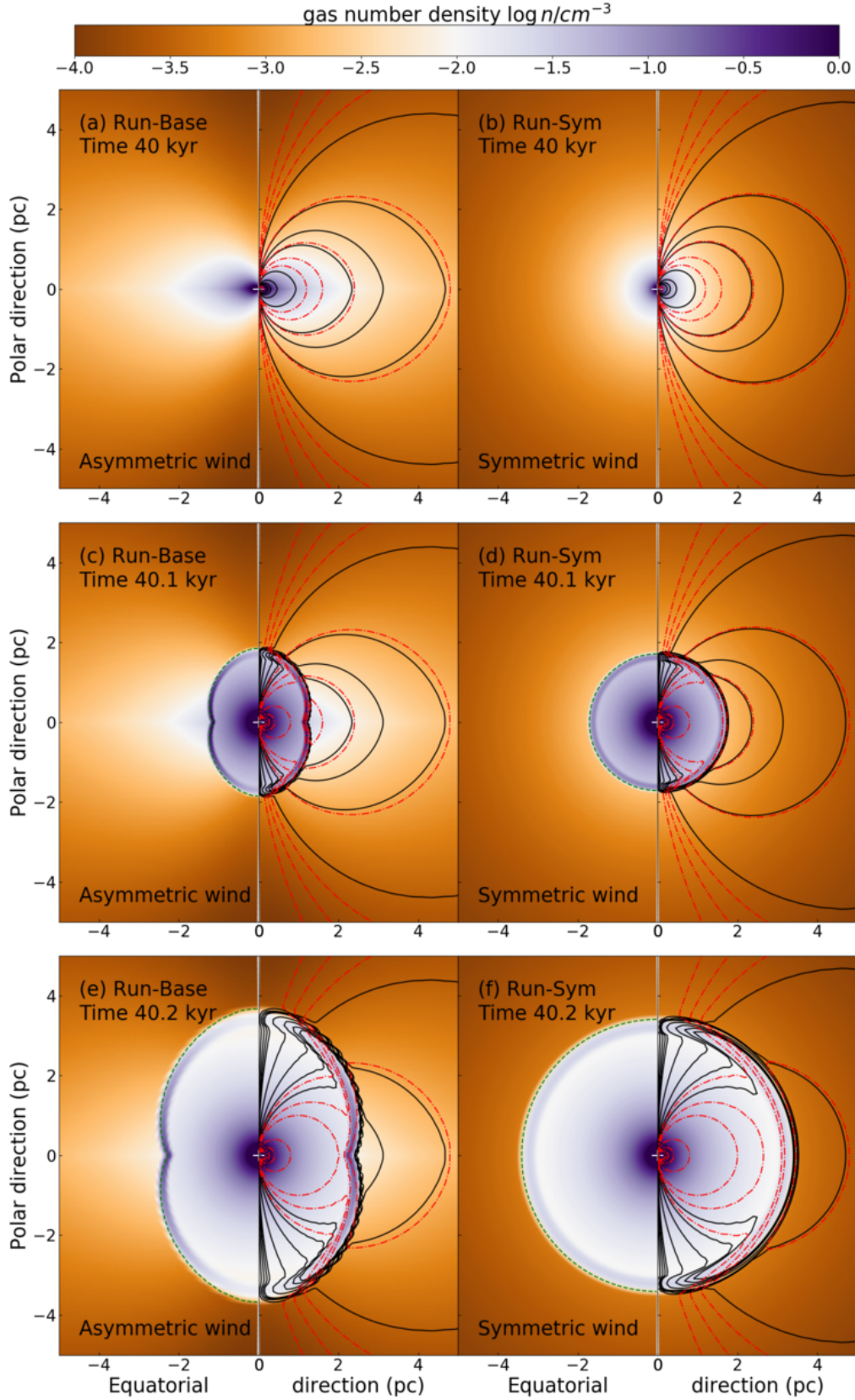


Figure 1. Number density field in our simulation models Run-Base (a) and Run-Sym (b). The dashed green contour is the tangential discontinuity of the Wolf-Rayet nebula, i.e. the location of the nebula made of equal proportion of blue supergiant and Wolf-Rayet stellar winds, where the passive scalar $Q = 0.5$. The solid black and dashed-dotted red contours on the right-hand part of each panels represent isovalues of the toroidal component of the velocity v_ϕ and magnetic field B_ϕ , respectively. The white cross marks the position of the star.

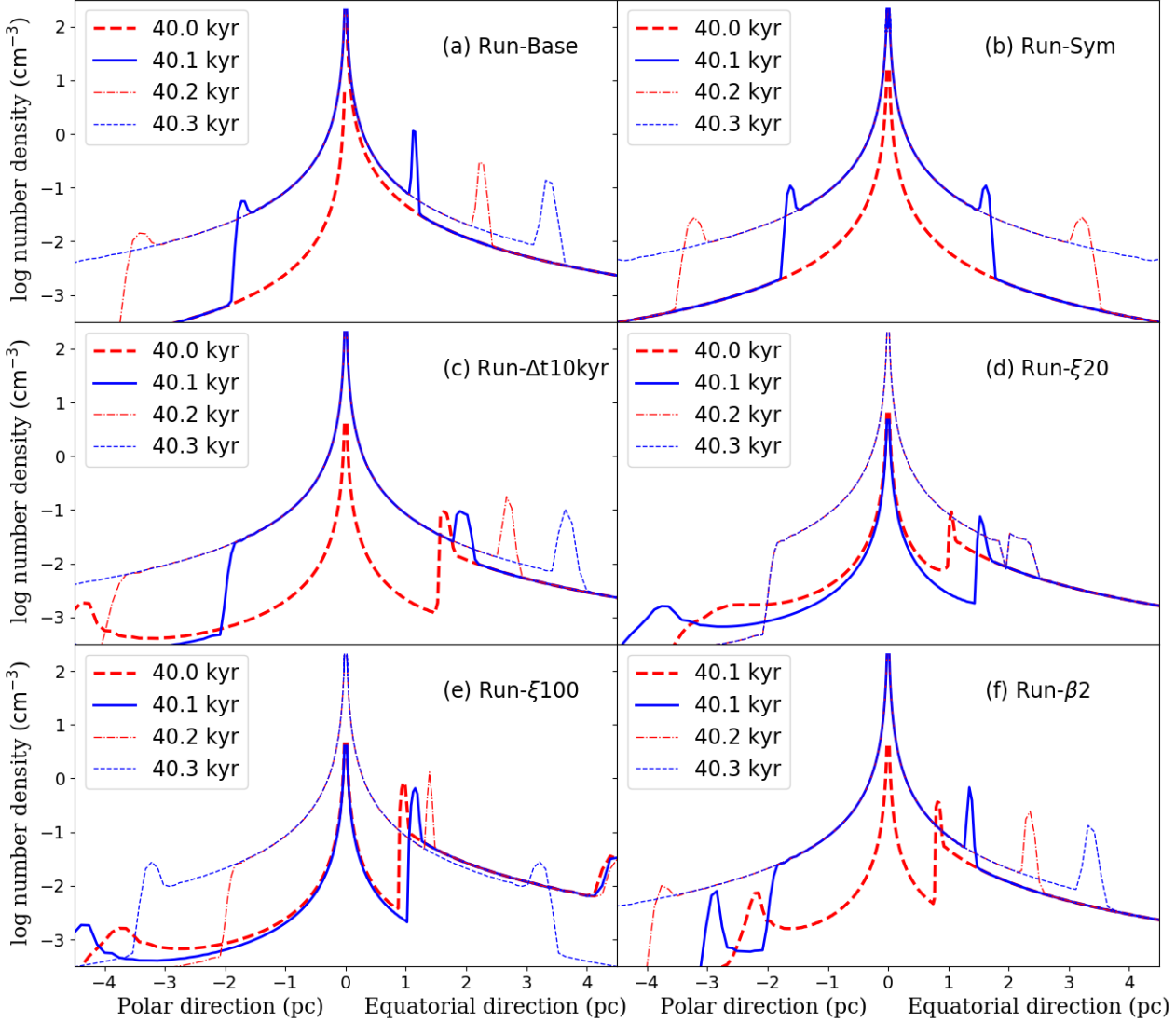


Figure 2. Cross-sections in the density field and toroidal magnetic field of the evolving Wolf-Rayet nebula. The panels correspond to different simulations, and on each panel the cross-section are plotted for both directions along the polar (left) and equatorial (right) directions of the domain.

blue supergiant stellar properties are as follows. We use $\dot{M}^{\text{bsg}} = 10^{-6} M_{\odot} \text{ yr}^{-1}$, which is of the order of magnitude of that of Sher 25 (Smartt et al. 2002), $v_{\text{w}}^{\text{bsg}} = 500 \text{ km s}^{-1}$, that is consistent with the values for HD 168625 ($350 \pm 100 \text{ km s}^{-1}$, Mahy et al. 2016) and for Sk-69°279 ($800 \pm 100 \text{ km s}^{-1}$, Gvaramadze et al. 2018). The stellar radius is $R_{\star}^{\text{bsg}} = 20 R_{\odot}$, which is that of Sk-69°279 ($800 \pm 100 \text{ km s}^{-1}$, Gvaramadze et al. 2018), and $v_{\text{rot}}^{\text{bsg}} = 60 \text{ km s}^{-1}$ (Mahy et al. 2016). The surface magnetic field of the blue supergiant ancestor star is taken to be $B_{\star}^{\text{bsg}} = 1 \text{ G}$, which is of the order of the magnetic fields observed in other cool stars (Kervella et al. 2018; Vlemmings et al. 2002, 2005).

The toroidal component of the stellar magnetic field is scaled with the value for the solar wind measured at 1 au (Herbst et al. 2020; Scherer et al. 2020). The Wolf-Rayet stellar properties are as follows. We use $\dot{M}^{\text{wr}} = 10^{-4.3} M_{\odot} \text{ yr}^{-1}$, $v_{\text{w}}^{\text{wr}} = 1900 \text{ km s}^{-1}$, $R_{\star}^{\text{wr}} = 2.3 R_{\odot}$ and $v_{\text{rot}}^{\text{wr}} = 10 \text{ km s}^{-1}$, respectively. These quantities are the values of the Wolf-Rayet star WR1 (WN4). Our stellar parameters are summarised in Table 1. The stellar surface magnetic

field is rather unconstrained, and we decided to take $B_{\star}^{\text{wr}} = 100 \text{ G}$. Similarly, we assume that the toroidal component of the magnetic field scales with the magnetic field in the solar wind (Herbst et al. 2020; Scherer et al. 2020).

In this work, we use our toy model to explore the effects of the progenitor stellar wind and phase transition properties on the shaping of the Wolf-Rayet nebulae. The simulation models are summarized in Table 2.

2.5 Radiative transfer calculations

As most circumstellar nebulae around evolved massive stars have been observed in the (near)-infrared waveband, we consequently desire, in order to discuss our models in the context of real data, to know how our simulated objects would look like if observed at that particular waveband. We perform radiative transfer calculations of our MHD simulation outputs against dust opacity using the RADMC-3D code (Dullemond 2012). Dust density fields are con-

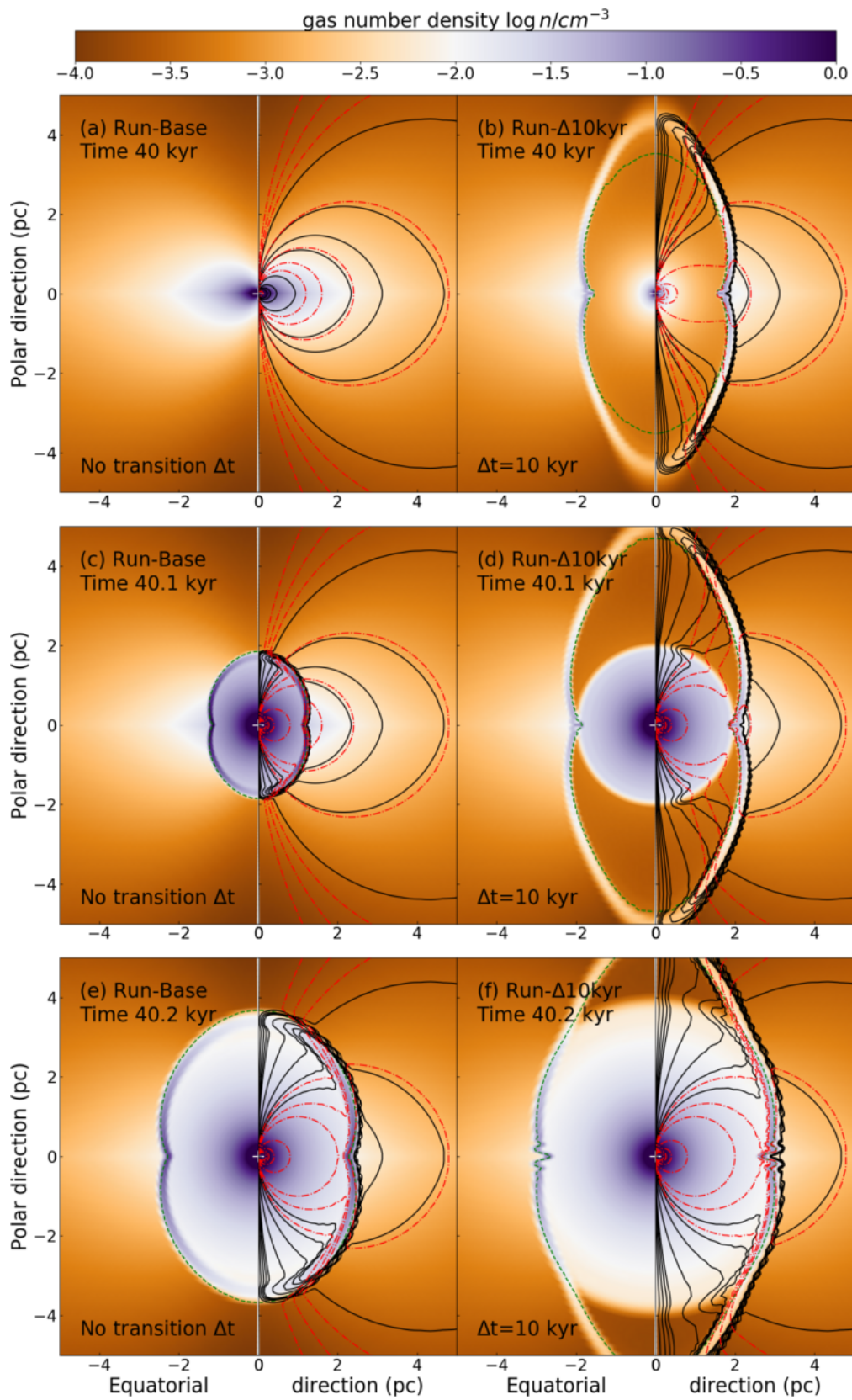


Figure 3. Same as Fig. 1 with our models Run-Base and Run- Δt 10kyr, exploring the effect of a phase transition timescale $\Delta t \neq 0$.

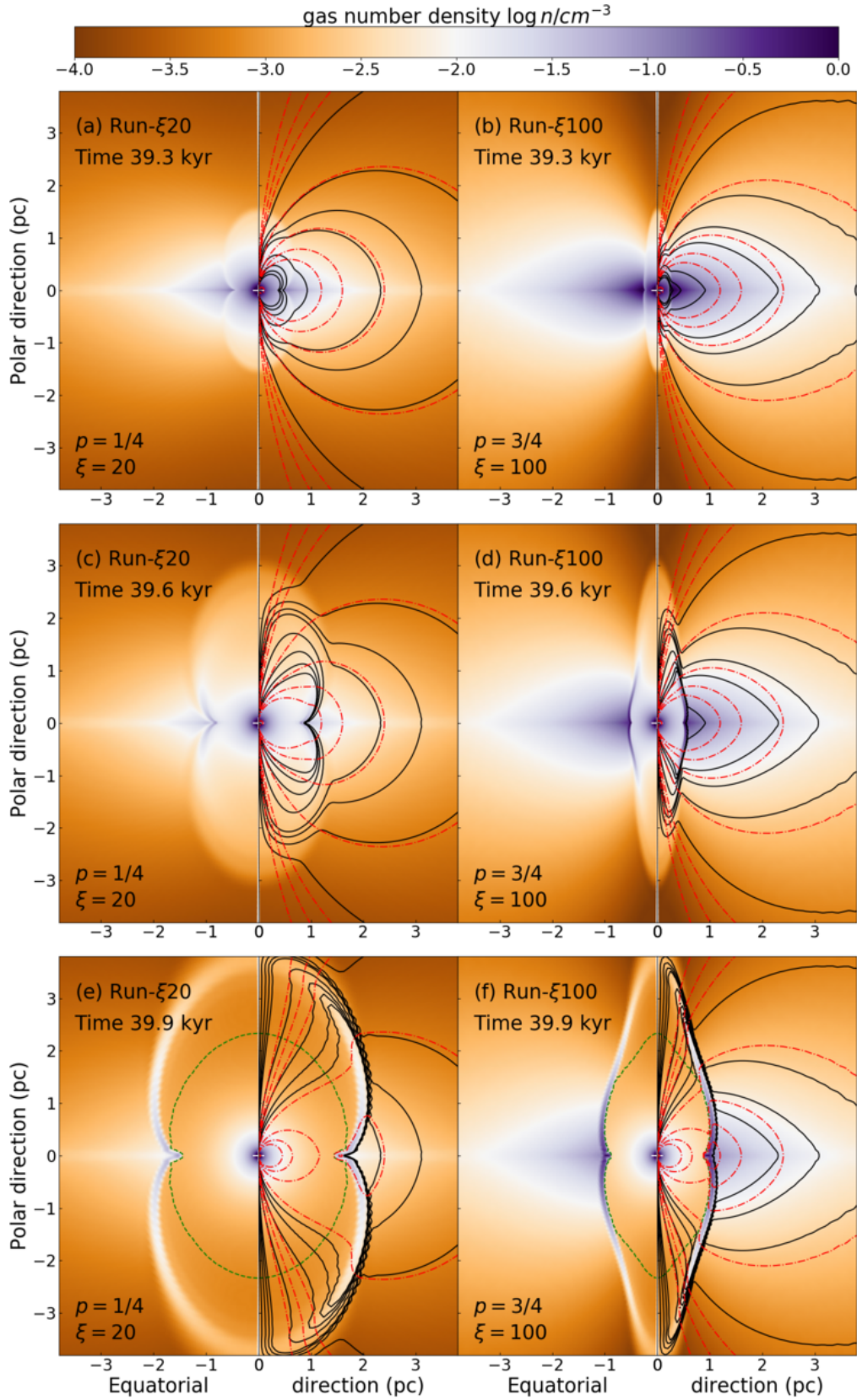


Figure 4. Same as Fig. 1 with our models Run- $\xi 20$ and Run- $\xi 100$, exploring the effect of the flattening degree ρ and density ratio ξ of the progenitor wind.

structured by assuming a standard gas-to-dust ratio of 1/200 and it is imported into RADMC-3D. The dust temperature is simulated by Monte-Carlo calculation using the algorithm of Bjorkman & Wood (2001) and photon packages are ray-traced from the stellar atmosphere to the stellar wind nebulae. The $24\ \mu\text{m}$ near-infrared emissivity is estimated using the Silicates dust opacity of Laor & Draine (1993) and it is projected onto the plane of the sky according to a particular selected viewing angle. The irradiating central massive star is assumed to be a spherical black body radiator of effective temperature T_{eff} that is taken as,

$$T_{\text{eff}}(t) = \begin{cases} T_{\text{eff}}^{\text{bsg}} & \text{if } t \leq t_{\text{wr}} - \Delta t, \\ \Delta T_{\text{eff}}(1 - F) + T_{\text{eff}}^{\text{wr}} & \text{if } t_{\text{wr}} - \Delta t < t \leq t_{\text{wr}}, \\ T_{\text{eff}}^{\text{wr}} & \text{if } t > t_{\text{wr}}, \end{cases} \quad (28)$$

where $\Delta T_{\text{eff}} = |T_{\text{eff}}^{\text{wr}} - T_{\text{eff}}^{\text{bsg}}|$. The stellar radius $R_*(t)$ is determined from Eq. 25. The hot, Wolf-Rayet material is distinguished from the cold blue supergiant gas using the passive scalar tracer of Eq. 27. We produce emission maps for a distance to the stellar source of 1 kpc, that is typical for massive star-forming regions.

3 RESULTS

This section presents the results from the modelling of Wolf-Rayet gas nebulae of blue supergiant ancestors. We compare the effects of the asymmetries and evolutionary phases of various pre-Wolf-Rayet stellar winds on the geometry of the gas nebulae.

3.1 Wolf-Rayet nebulae of asymmetric versus spherical blue supergiant wind

In Fig. 1 we plot the number density field in our baseline simulation Run-Base (left column of panels) and our model Run-Sym (right column of panels), which assume asymmetric and isotropic blue supergiant progenitor stellar winds, respectively. The dashed green contour is the tangential discontinuity, where blue supergiant and Wolf-Rayet stellar winds are in equal proportions ($Q = 0.5$). Solid black and dashed-dotted red contours trace v_ϕ and B_ϕ , respectively, and the white cross marks the position of the star. The model Run-Sym obviously generates a spherical nebula (Fig. 1d,f) by fast-wind-slow-wind collision, as modelled in the work of Meyer et al. (2020). In model Run-Base the asymmetric blue wind is expelled as a torus of outflowing material, see the studies of Raga et al. (2008) and Fang et al. (2017), respectively, onto which stellar rotation and a Parker wind is superposed (Fig. 1a). Both models have no phase transition, therefore, the Wolf-Rayet stellar wind directly interacts with the luminous blue supergiant stellar wind. The initial spherically-symmetric stellar wind of Run-Base is channelled by its surroundings and adopts a bipolar morphology (Fig. 1c,e). One clearly sees magnetic dipoles in both the old slow and new fast winds, whose field lines are compressed in the shell region. Given the size of the nebula ($\leq 10\ \text{pc}$), the asymmetric nebulae can develop inside of the region bordered by the termination shock of the main-sequence stellar wind bubble (Meyer et al. 2020). These rings should therefore form even in the context of the supersonic bulk motion of the driving blue supergiant star (Fig. 1b,d,f). This mechanism is therefore the MHD equivalent of the young aspherical Wolf-Rayet nebulae of red supergiant stars of Brighenti & D’Ercole (1997), this time in the context of a blue supergiant ancestor.

Fig. 2 shows cross-sections taken through the number density field of the Wolf-Rayet nebulae. The figure plots the cross-sections, taken at intervals of 0.1 kyr through several characteristic simulation snapshots of the blue supergiant to Wolf-Rayet phase transition event. The left-hand part of each panel corresponds to the polar direction, whereas the right-hand part of the panels corresponds to the equatorial plane of the nebulae. The spherical nebula in Run-Sym (Fig. 2b) is obviously similar along both the polar and equatorial directions. The shell of swept-up blue wind grows under the effect of the expelled Wolf-Rayet momentum and the contrast in density along both direction decreases, i.e. the post-shock density of the Wolf-Rayet nebulae diminishes with time and so does the corresponding emission (see Section 4.2). At time 40.1 kyr, the cross-sections of the asymmetric model Run-Base exhibit clear differences between the polar and equatorial directions (Fig. 2a), as a result of the wind asymmetry. When the Wolf-Rayet material begins to blow, the shell of swept-up supergiant gas is denser in the equatorial plane than in the direction perpendicular to the equator, see thick blue and thin lines of Fig. 2a. This latitude-dependent density contrast is at the origin of the asymmetric character of some observed Wolf-Rayet nebulae.

3.2 Effects of the phase transition timescale

Fig. 3 compares the density fields in our simulation models Run-Base (left panels) and Run- Δt 10kyr (right panels), which differs by the blue supergiant to Wolf-Rayet phase transition interval. Such transition period is non-existent in model Run-Base while it is $\Delta t = 0.1\ \text{kyr}$ in model Run- Δt 10kyr. Our phase transition timescale is in accordance with both the typical duration of luminous blue phases $\sim 10^4\ \text{yr}$ and with the timescale of blue-to-red phase transition (Mackey et al. 2012; Groh et al. 2014). The Wolf-Rayet nebula in Run-Base is generated by the simultaneous changes of the wind velocity and density, engendering a peanut-like morphology, which shocked layer accumulates compressed magnetic field lines, as described in Section 3.1. In Run- Δt 10kyr the stellar wind velocity increases first, provoking a more elongated jet-like nebula, before that the sudden changes in wind density fills it with denser, isotropic Wolf-Rayet material (see Eq. 21-23). In the latter case, Rayleigh-Taylor instabilities form in the equatorial plane, as a consequence of the wind-wind collision at work therein, see the discussion in Brighenti & D’Ercole (1997). This comparison shows that the properties of the time windows during which the wind properties evolve has a little influence on the overall appearance of Wolf-Rayet nebulae. Our simplistic setup uses analytic prescriptions that mimic the evolution of the central massive star, hence, the detailed shape of the nebula might be slightly different with more realistic, time-dependent stellar wind prescriptions, e.g. using pre-computed evolutionary tracks (Brott et al. 2011).

In model Run- Δt 10kyr, the accelerating stellar wind has already interacted with the dense equatorial blue supergiant wind, resulting in a bipolar shell (Fig. 3a,b) that is later filled by the Wolf-Rayet wind. The wind-wind interaction is stronger for a reduced phase transition interval Δt (Fig. 3a,c), while the density of the shocked material in Run- Δt 10kyr is reduced, as a consequence of the diminished wind momentum at the moment just before the sudden changes in mass-loss rate at t_{wr} . Nevertheless, in both models, the Wolf-Rayet wind eventually melts with the shell of swept-up blue supergiant material, and, comparable equatorial densities are reached (Fig. 3a) as it expands outwards (Fig. 3c). Finally, once the hot gas filled the bipolar cavity, both nebulae have similar overall dimensions except at the poles, where the magnetic field lines are

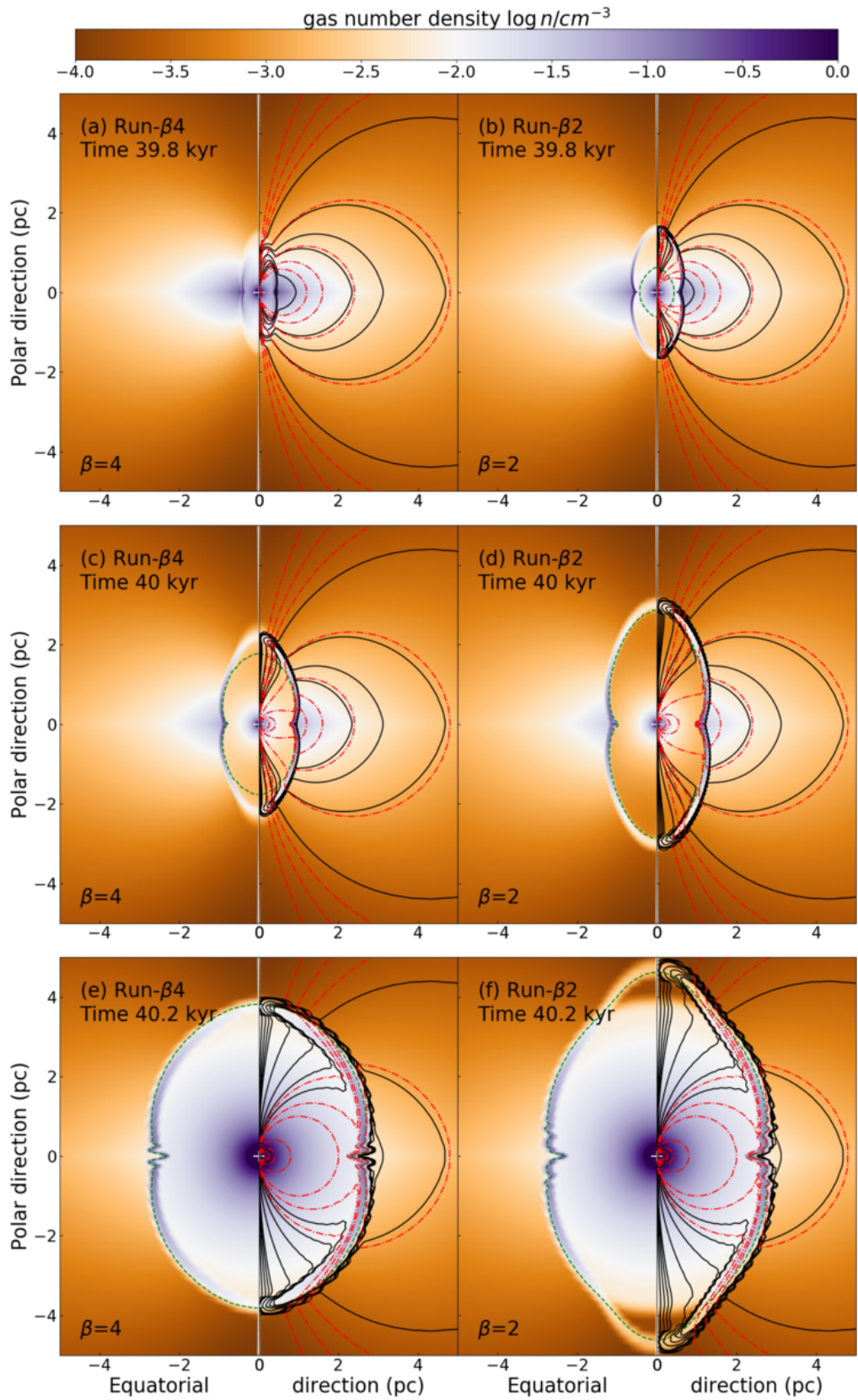


Figure 5. Same as Fig. 1 with our models Run- β_4 and Run- β_2 , exploring the effects of the interpolation exponent β during the phase transition.

collimated (Fig. 3d). This further illustrates that the morphology of older asymmetric Wolf-Rayet nebulae is governed by the surface characteristics and stellar wind properties, such as terminal velocity and mass-loss rate of the ancestor stars, as well as the manner in which the evolutionary phase transition happens, but not by the ambient medium properties.

3.3 Effects of the blue supergiant stellar wind asymmetries

Fig. 4 compares two simulation models, Run- $\xi 20$ and Run- $\xi 100$, both with the same phase transition timescale $\Delta t = 10$ kyr, but different density flattening degrees towards the equator p and density equator-to-pole ratios ξ , namely, $p = 1/4$ and $\xi = 20$ (Run- $\xi 20$) and $p = 3/4$ and $\xi = 100$ (Run- $\xi 100$), respectively. The different pre-Wolf-Rayet morphologies of the circumstellar medium profoundly impact the development of the shell generated by wind-wind interaction between blue supergiant to the Wolf-Rayet winds. The denser the material in the equator, the more collimated the Wolf-Rayet stellar wind (Fig. 4b), as a result of the thicker disc-like blue supergiant distribution (Fig. 4a). On the other hand, the simulation with a thinner equatorial plane produces a peanut-like nebula, recalling the mechanisms for the shaping of the homunculus of η -Carina (Langer et al. 1999; González et al. 2004; Hirai et al. 2021). Note the gradual opening of the magnetic field lines as the wind speed accelerates (Fig. 3a-e,b-f). Again, this is mostly shaped by the blue supergiant wind whose velocity gradually increases during the phase transition up to reaching the fast values of the Wolf-Rayet star (black dotted line in Fig. 4c,d). The discrepancy between peanut-like and jet-like Wolf-Rayet nebulae persists at later times, when the stellar phase transition keeps going (Fig. 4e,f).

As soon the Wolf-Rayet stellar wind interacts with the walls of the nebula, the wind-wind interface becomes naturally much denser in the model with $\xi = 100$ than in the case with $\xi = 20$ (Fig. 4c,d). This reflects in the cross-sections taken through the density fields of the simulations (Fig. 4d,e). Indeed, the model with $\xi = 20$ produces a larger shell in the equatorial plane, whereas that with $\xi = 100$ is more compact, thinner and also much denser. The density jump at the expanding front is larger at time 40.1 kyr in our model Run- $\xi 100$, than in our simulation Run-p1/2 and it stalls at ≈ 1 pc from the star, whereas the other nebula in Run-p1/2 is more enlarged in the equatorial plane. The flattening degree of the density towards the equator and the equator-to-pole density ratio turns to be a major parameter in the shaping of Wolf-Rayet nebulae, as it controls their final aspect ratio and therefore their overall morphology. Within the explored parameter space, we therefore produce either peanut-like or jet-like shapes.

3.4 Effects of phase transition properties

Our last series of comparison tests consist in changing the interpolation between the blue supergiant and Wolf-Rayet stellar surface properties during the phase transition. It is governed by the exponent parameter β in Eq. 22, set to $\beta = 2$ in our model Run- $\beta 2$ (linear interpolation) and to $\beta = 4$ in our Run- $\beta 4$ (squared polynomial interpolation). The transition phase timescale is set to $\Delta t = 5$ kyr. In Fig. 5a and Fig. 5b, the pre-shaped circumstellar medium in which the Wolf-Rayet star blows its material is similar, and how the blue supergiant stellar wind gradually adopts a faster speed is the only effect responsible for differences in the nebula's morphologies. This keeps on going for another 0.1 kyr, until the tangential discontinuity between the two colliding winds

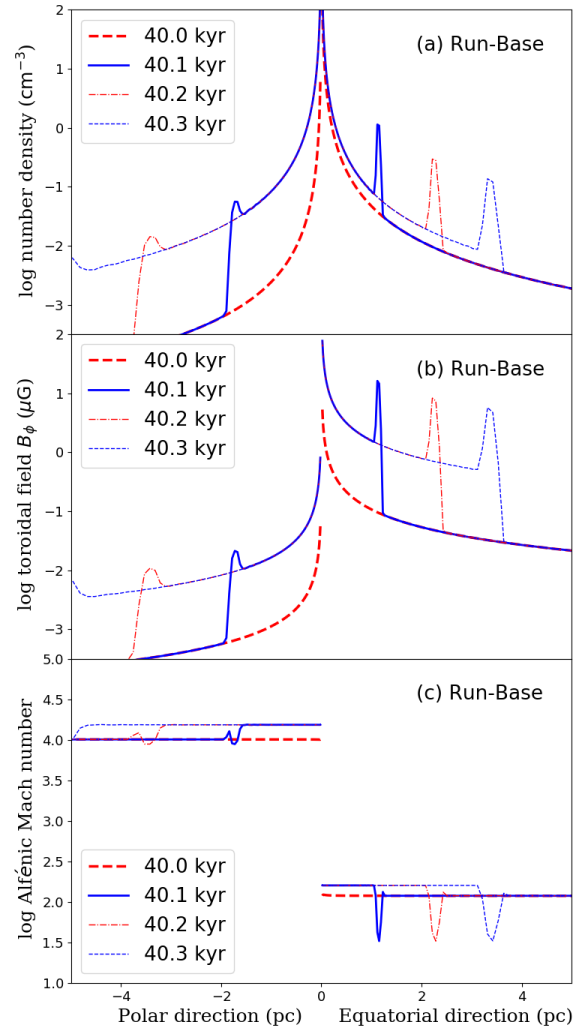


Figure 6. Cross-sections in the density field (top panel), toroidal magnetic field (middle panel) and Alfvénic Mach number (bottom panel) of the evolving Wolf-Rayet nebula in our simulation Run-Base. On each panel the cross-section are plotted for both the polar (left) and the equatorial direction (right) of the computational domain.

reaches the cavity. Nevertheless, when the full Wolf-Rayet wind blows through and fully fills the cavity, morphological differences are rather small (Fig. 5e,f). The field lines are opened under the effect of the faster equatorial rotation of the Wolf-Rayet star. Instabilities developing in the equatorial plane, as in model Run- $\Delta t 10$ kyr, appear in both runs, despite of the different, longer phase transition. The apex of the polar lobes remains the only trace of the different stellar evolution history of the final Wolf-Rayet stars.

3.5 Magnetic properties of the Wolf-Rayet nebulae

In Fig. 6a we plot a time evolution series of cross-sections taken through the number density field (top panel) in our simulation model assuming an aspherical blue supergiant stellar wind (Run-Base). The selected times correspond to the moment the Wolf-Rayet wind begins blowing into the blue supergiant material. Fig. 6b (middle panel) displays cross-sections taken at the same time instances and location, through the toroidal density field B_ϕ (in μG) and plotted in the logarithmic scale. One sees that the mag-

netic field in the Wolf-Rayet nebula, governed by its toroidal component is maximum in the region of the expanding shell. The compression factor of the magnetic stellar wind field reflects that of the expanding shell density (Fig. 6a,b), and, inversely, the toroidal field B_ϕ is weaker along the polar direction. Fig. 6c (bottom panels) plots the Alfvénic Mach number in the circumstellar nebula. The gas is super-Alfvénic everywhere, with lower values $M_A \sim 1.5$ in the region of the equatorial plane, in the compressed shell, and it peaks at $M_A \approx 4$ along the polar direction.

In Fig. 7 we display scatter plots for the distribution of gas in the computational domain, representing the number density (in cm^{-3}) of the wind as a function of its velocity (in km s^{-1}), coloured by the value of the toroidal magnetic field B_ϕ (in μG). The different panels of the figure correspond to several time instances of the simulations, from the younger (top panels) to the older times (bottom panels), and each column represent a simulation model. The constant, isotropically freely-streaming stellar wind of the blue supergiant progenitor is represented by an horizontal line of decreasing toroidal magnetic field from the high to the lower densities (Fig. 7a,b). When the star evolves to the Wolf-Rayet phase, the horizontal is split into two horizontal lines of different velocities, a fast velocity, high density one (the Wolf-Rayet component), and a slow, low-density one (the blue component), see Fig. 7c. The model Run-Base with anisotropic stellar wind vertically spreads the horizontal line of Fig. 7a as a broadened band, whose height is a function of the degree of flattening of the wind and of the equator-to-pole density ratio, see Fig. 7d,e. The phase transition, with spherical Wolf-Rayet wind blown into an asymmetric blue supergiant wind, shifts the high density part of the bar-like distribution to a higher velocity, higher number density horizontal line (Fig. 7f). The region between the two winds exhibits variations of the toroidal magnetic field from the density compression during the wind-wind interaction, which results in more scattering of the data in the velocity-density plane (Fig. 7f).

The model with both anisotropic pre-Wolf-Rayet stellar wind and long phase transition timescale, Run- $\Delta t10\text{kyr}$, exhibits a distribution in the ρ - v diagram both reporting the initial freely-expanding, high-density stellar wind as a high-density horizontal bar, plus a low-density region broadened in velocity, as a result of the blue supergiant asymmetries, already at work at that time (Fig. 7g). At later times, the transition region greatly affects the gas properties in the equatorial plane and this results in a larger toroidal magnetic field (Fig. 7h,i). At even later times, the development of instabilities at the wind-wind interface in the equatorial plane strongly disperses the high-velocity gas in the ρ - v diagram (Fig. 7i). Similarly, the simulation with Run- $\xi100$ exhibits a more important scattering of the magnetised blue supergiant and expanding Wolf-Rayet stellar winds. The velocity broadening is strong, as a result of the large equator-to-pole density ratio ξ . The jet-like nebula has a dispersion of the material therein that contains highly-magnetised, swept-up, slow diluted blue supergiant stellar wind in the equatorial plane (Fig. 7k,l). The different velocity distributions in peanut-like ($\xi = 20$) and jet-like ($\xi = 100$) Wolf-Rayet nebulae clearly appear as a consequence of the aspect ratio of the wind bubble, see Fig. 7i,l.

Fig. 8 shows our models Run- $\beta4$ and Run- $\beta2$, respectively, which differ by the manner the various quantities of the stellar wind are interpolated during the phase transition. At time 40 kyr both nebulae have already grown when the new-born Wolf-Rayet wind is blown into the accelerated blue supergiant wind, as testifies the S-shape in the density-velocity plane. The distribution of the gas therein presents both the broadened low-velocity compo-

nent from an equatorially-asymmetric blue supergiant stellar wind and the horizontally-distributed component of a rapid Wolf-Rayet wind. Both distributions with changing β are qualitatively similar (Fig. 8a,b), while differences at the transition between the two components appear, as the wind-wind interaction region at the equatorial plane is not the same. The model with non-linear interpolation ($\beta = 4$) reveals compressed gas with a stronger magnetisation B_ϕ . The phase transition continues modifying the curved, S-shaped region of scattered dots between the two components of the ancestor and evolved stellar winds. Such curvature is more pronounced in the case with $\beta = 4$ because the wind momentum increases faster with the polynomial interpolation than in the linear case with $\beta = 2$, which results in an accumulation of dense, magnetised and fast material in the equatorial plane (Fig. 8c,d). The high velocity component turns into a thin horizontal line once the Wolf-Rayet wind is fully established. The instabilities developing in those peanut-like Wolf-Rayet nebulae are responsible for the scattering of points in the high-density, high-velocity parts of the diagram.

4 DISCUSSION

This section discusses the caveats of our method and compares our study to results in precedent works. We also discuss the infrared emission properties of the young Wolf-Rayet wind nebulae, and, finally, we compare our results with observations.

4.1 Model limitations

The very first caveat of our simulations is their 2.5-dimensional nature, as our method naturally imposes axisymmetry to the Wolf-Rayet nebulae (Heiligman 1980; García-Segura et al. 1999). While this is acceptable in our pilot study, performing full 3D MHD models better resolving the detailed formation of, e.g. instabilities during the wind-wind interaction mechanisms (Brighenti & D’Ercole 1997; Meyer et al. 2020) should be considered in the future. Secondly, we neglected several microphysical processes, such as radiation transport in the close surroundings of the massive star. The high temperatures of the Wolf-Rayet star ($\sim 10^5$ K) must affect the local thermodynamical properties and the energy budget of the stellar wind, and, as radiation pressure is at work therein, this should change the gas dynamics (Moens et al. 2021). Any chemical and/or non-ideal MHD mechanisms are also totally neglected in our simulations. Their consideration, much beyond the scope of our simplistic work, will be treated in follow-up studies. Last, our study which continues the work of Brighenti & D’Ercole (1997), utilises analytic prescriptions for the evolution of the stellar wind properties. It has the advantage to directly use stellar properties derived from e.g., observations of blue supergiant stars (Smartt et al. 2002; Mahy et al. 2016; Smith 2017; Gvaramadze et al. 2018), however, at the cost of the introduction of free parameters such as the timescale Δt of the corresponding phase transition. This can be circumvented by using self-consistently calculated theoretical stellar evolution models (Brott et al. 2011; Szécsi et al. 2020).

4.2 Infrared emission maps

In Fig. 9 we display $24\mu\text{m}$ emission maps calculated on the basis of our Wolf-Rayet nebula model Run-Base, using the RADMC-3D code. The surface brightness is plotted in the linear scale

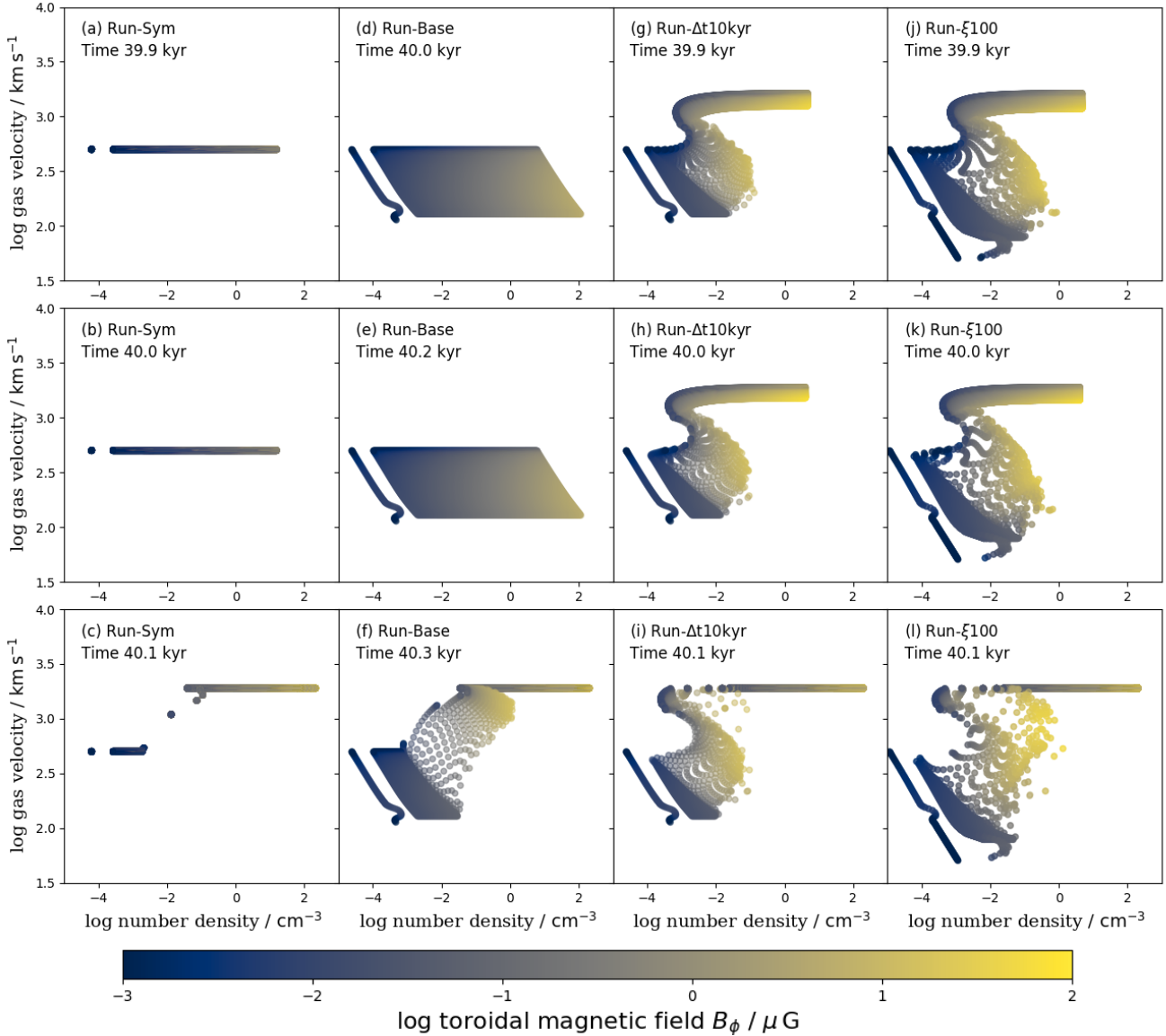


Figure 7. Correlation between the number density and the velocity of the gas in the inner 5 pc of the computational domain, for several simulations of the stellar wind nebulae generated during blue supergiant to Wolf-Rayet phase transitions, with colours representing the strength of the toroidal of the magnetic field B_ϕ .

in $\text{erg cm}^2 \text{s}^{-1} \text{arcsec}^{-2}$ for several viewing angles and the images are calculated excluding the hot dust-free Wolf-Rayet gas, see Meyer et al. (2020). On each panel the central white cross marks the position of the star. The first column of panels displays the time-dependent edge-view evolution of the close circumstellar medium of the massive stars. Before the evolution of the blue supergiant star, the asymmetric wind generates a bright oblate disc-like shape extending in the equatorial plane of the star (Fig. 9a). This model does not have a long phase transition interval Δt , and the hot Wolf-Rayet wind directly interacts with the dense equatorial colder gas. This interaction region emits in the mid-infrared, which produces the bipolar morphology (Fig. 9d). As the phase transition ends, the nebula further extends and become fainter at the poles, while conserving its overall bipolar bubbly shape. The second column of panels plots the same sequence of images considered with an inclination angle $\theta = 45^\circ$ with respect to the plane of the sky.

The situation is qualitatively the same as for $\theta = 0^\circ$, except that the bright infrared equatorial ring appears as an ellipse (Fig. 9e,h). The last column of panels displays top-viewed nebulae, which, as a consequence of the 2.5D nature of the simulations, look like rings extending away from the evolving central star (Fig. 9f,i). The maximum emission region is the interaction layer where the Wolf-Rayet wind reaches the termination shock of the blue supergiant nebula (Fig. 9d,e,f).

Fig. 10 is as Fig. 9 for the other simulations models listed in Table. 1. The left column of panels shows the nebula when the wind-wind collision begins, while the right column of panels shows the circumstellar nebula around the Wolf-Rayet stars at a later time. Both series of images are displayed with a viewing angle of $\theta = 45^\circ$ with respect to the plane of sky. The model Run-Δt10kyr has a phase transition $\Delta t = 10 \text{ kyr}$ extending the time interval during which the Wolf-Rayet wind merges with the previous blue

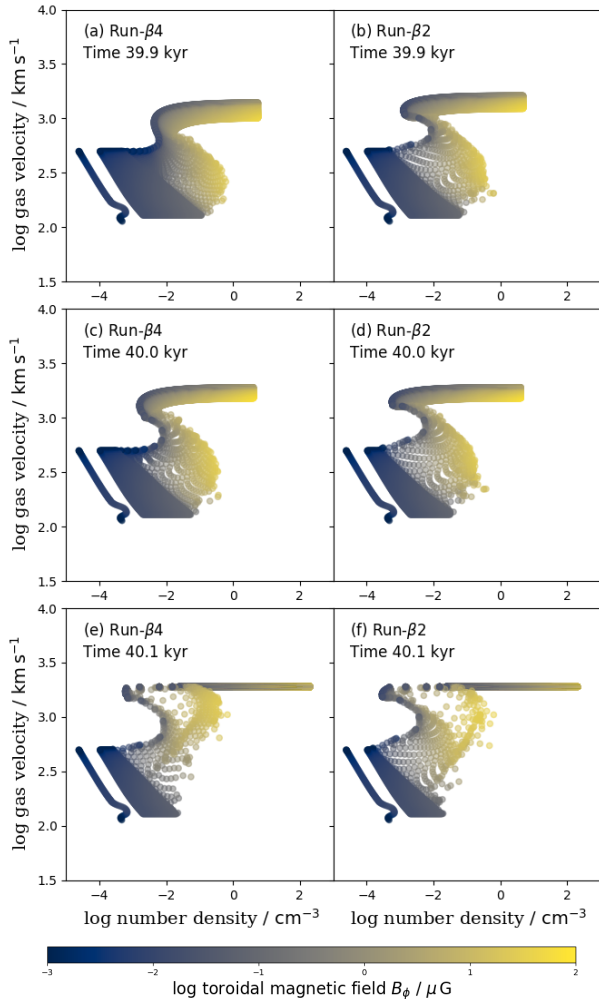


Figure 8. Same as Fig. 7 for our models Run- $\beta 4$ and Run- $\beta 2$.

supergiant material. This results in a denser region of wind-wind interaction and a brighter bipolar nebula (Fig. 10a) materialised as an ellipsoid in the projected equatorial plane (Fig. 10b). Our model Run- $\xi 20$ has a different density flattening degree towards the equator. It emphasizes the bipolar aspect of the nebula, which is less bubbly and more elongated (Fig. 10c,d). Our model Run- $\xi 100$ with a larger equator-to-pole density ratio $\xi = 100$ generates a tubular nebula as during the phase transition the wind material is channeled into the direction perpendicular to the equator, resulting in a less compressed and $24 \mu\text{m}$ -fainter expanding shell. The model Run- $\beta 4$ with a non-linear interpolation of the stellar wind quantities during the phase transition produces a quicker and more violent wind-wind collision and a brighter interaction region (Fig. 10g,h). Our model Run- $\beta 2$ with a linear interpolation induces a more important compression of the shell of stellar wind, and also a more pronounced bipolar morphology (Fig. 10i,j).

4.3 Comparison with observations

4.3.1 Generalities

The geometry of Wolf-Rayet nebulae is a long-standing problem and still rather unexplored mystery. All except one simulation performed to date predict their appearance to be both spher-

ical and affected by hydrodynamical instabilities originating from the evolved Wolf-Rayet stellar wind, blown into the interior of its own main-sequence stellar wind bubble and interacting with the shell generated during its previous, e.g. red supergiant, evolutionary stage (Freyer et al. 2003, 2006; Toalá & Arthur 2011; Meyer et al. 2020). All these models assume a static massive star undergoing a succession of isotropically-launched stellar winds. As discussed above, a cool, dense stellar wind launched along the equator of the star can make the Wolf-Rayet nebula strongly anisotropic, shaping the outflow as a bipolar structure. The physical origin of the equatorial stellar wind is so-far included as sub-grid models in the few simulations run so far, see Brighenti & D’Ercole (1997). Our study is therefore the first work continuing that on asymmetric Wolf-Rayet nebulae of Brighenti & D’Ercole (1997).

The previous paper of our series explored the effects of the stellar bulk motion on the formation of Wolf-Rayet stars. Indeed, the fastest runaway massive stars of the Milky Way are strong-winded and bow-shock-free Wolf-Rayet stars carrying circular rings, which challenged our understanding of the formation of Wolf-Rayet nebulae (Meyer et al. 2020). A typical example is the nebula M1-67 around the star WR124 (van der Sluys & Lamers 2003). The proposed simple solution for their formation scenario teaches us that the stellar motion of the driving star does not influence the growth of Wolf-Rayet nebulae, since the region of free-streaming between stellar surface and main-sequence wind bubble’s termination shock is sufficiently extended. This is largely the case for high-latitude objects, as the diluted medium therein favors the production of huge and extended bow shocks, making room for wind-wind shell collision to happen without being affected by the ISM material. Importantly, the absence of observed ISM material in Wolf-Rayet nebulae (Fernández-Martín et al. 2012; Esteban et al. 2016) indicates that most Wolf-Rayet shells, including bipolar Wolf-Rayet nebulae, are probably produced this way, and, this further implies that the large-scale wind-blown bubble can be ignored when numerically modelling them.

However, the very complex shape of many observed Wolf-Rayet nebulae challenges this picture (Toalá et al. 2015). When exactly bipolarity happens and which factors are in control of this? Which progenitors are responsible for which kind of circumstellar nebulae? The well-studied bipolar Wolf-Rayet nebulae NGC 6888, of probable red supergiant ancestor, and RCW58, seemingly coming from a blue supergiant, are the ideal cases to test numerical models like ours against observations, see the discussion in Garcia-Segura et al. (1996) and Garcia-Segura et al. (1996). Bipolarity of single blue supergiant origin is the situation that we simulate in the present study, and it is in accordance with the interpretation of Garcia-Segura et al. (1996) in the context of RCW58. However, what can our result teach us regarding the other, red supergiant-based scenario?

4.3.2 What makes NGC 6888 asymmetric?

The gaseous nebula NGC 6888, also called the veil nebula, the crescent nebula, Caldwell 27, Sharpless 105, is an asymmetric wind bubble found around the evolved massive Wolf-Rayet WN66(h)-type star WR 136. Its particular shape is made of two bipolar lobes and of an equatorial ring of denser material. It has long been studied in great detail (Parker 1978; Treffers & Chu 1982; Garcia-Segura et al. 1996; Fernández-Martín et al. 2012; Mesa-Delgado et al. 2014; Toalá et al. 2014; Esteban et al. 2016; Rubio et al. 2020). Early observations of the surroundings of NGC 6888 revealed a variation of the level ionization, traced by the optical line

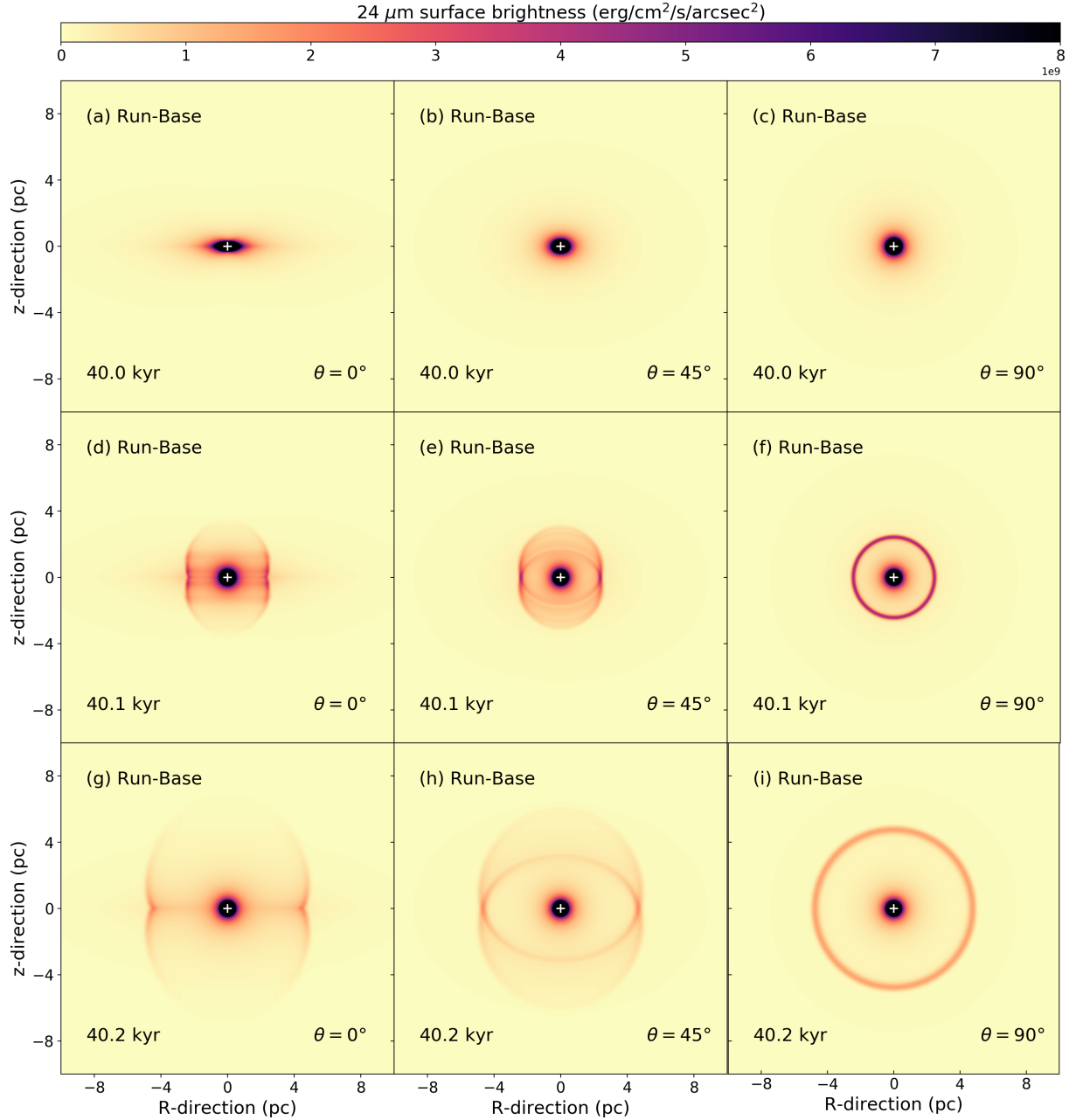


Figure 9. Emission maps of calculated from the Wolf-Rayet circumstellar nebulae model Run-Base. The figure plots the $24\ \mu\text{m}$ surface brightness (in $\text{erg cm}^2\ \text{s}^{-1}\ \text{arcsec}^{-2}$) of our Wolf-Rayet nebulae. Quantities are calculated excluding the non-dusty Wolf-Rayet material plotted with the linear scale, under several viewing angles θ . The white cross marks the position of the star.

ratios $[\text{NII}]/\text{H}\alpha$ in the many clumps along the surface of the shell, witnessing an efficient mixing of materials preceding the formation of the Wolf-Rayet shell (Parker 1978; Fernández-Martín et al. 2012). The presence of dust and enriched elements around Wolf-Rayet nebulae indicate that (i) they result from wind-wind interaction of evolved material, (ii) one of the evolved winds is that of a cold, dust-producing, supergiant phase of stellar evolution and (iii) the kind of detected dust tells us that the wind from a main-sequence star does not contribute to the shaping of the nebula. NGC 6888 has been the site of the first observation of the aftermath of the CNO cycle of nuclear reactions into the stellar core (Mesa-Delgado et al. 2014), and its progenitor star has been constrained to be a single, red-supergiant-evolving star of $25 - 40\ M_{\odot}$ (Stock

& Barlow 2014; Mesa-Delgado et al. 2014). Hence, these Wolf-Rayet stars must probably have undergone a red supergiant evolutionary phase, and, such scenario has been modelled using 1D and 2D spherically-symmetric hydrodynamical simulations in Garcia-Segura et al. (1996). However, it is clear that WR136 has been a cold star prior to the Wolf-Rayet phase (Stock & Barlow 2014), the origins of the progenitor’s asymmetries are still not understood.

Our results show that a non-eruptive single blue supergiant star can not spin sufficiently fast to produce an asymmetric pre-Wolf-Rayet circumstellar medium (our Fig. 1). Since red supergiants and other late-type stars do not rotate fast (Kervella et al. 2018; Vlemmings et al. 2002, 2005), their shells can not be greatly affected by rotational and/or magnetic effects either. Therefore, the

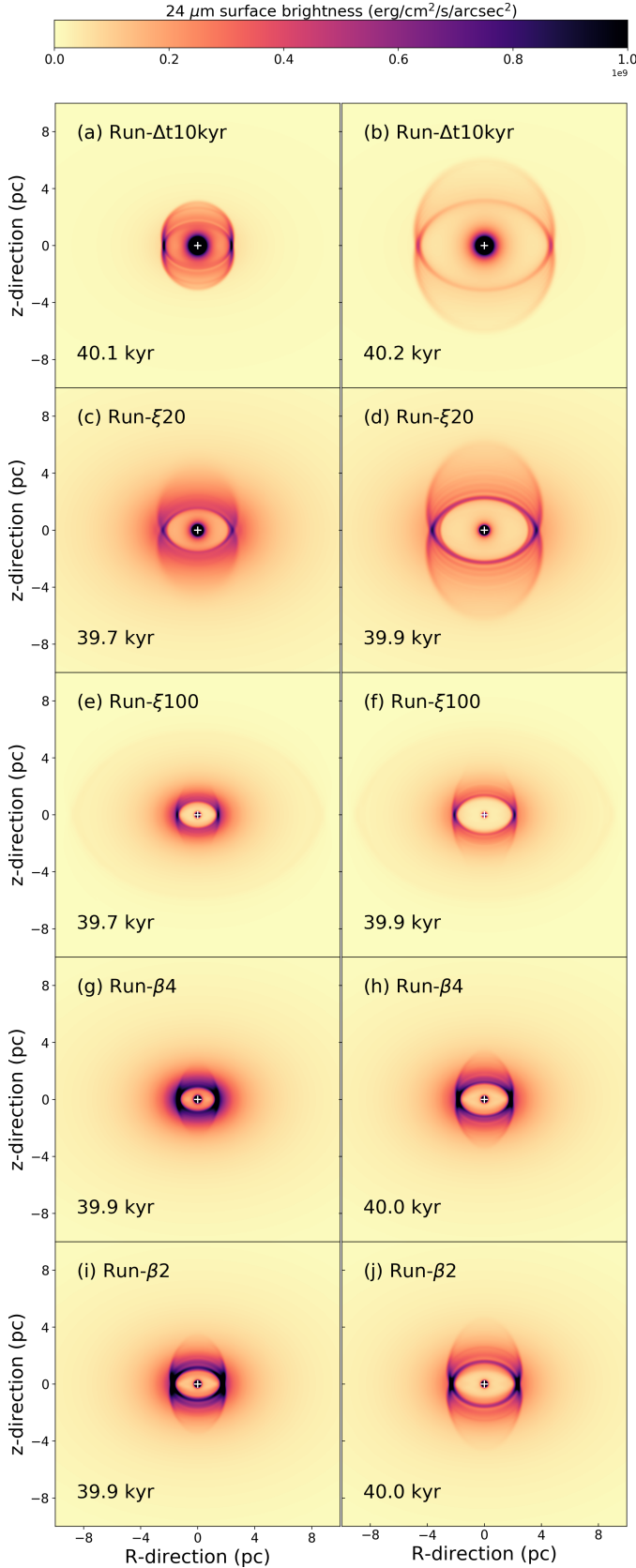


Figure 10. Same as Fig. 9 for our other models. Images assume an inclination angle of $\theta = 45^\circ$.

question is how NGC 6888 can produce a bipolar Wolf-Rayet nebula with an equatorial ring, obviously witnessing the existence of an equatorial structure produced during a post-main-sequence evolutionary phase prior to the Wolf-Rayet phase? The most accepted picture, supported by CNO yields measured in the nebula, made of a main-sequence, red supergiant and Wolf-Rayet single star evolutionary channel, is therefore challenged by our results, as explanations for the polar asymmetries of the pre-Wolf-Rayet wind are still missing.

We speculate that a mechanism, similar to that revealed for asymptotic giant stars, see particularly Decin et al. (2020) and Decin (2020), in which multiplicity generates a latitude dependence of the stellar wind, should be at work in the context of red supergiant stars as well, and in particular to the central star(s) of NGC 6888 before it adopted a Wolf-Rayet spectral type. Other possibility could be alternative evolution scenario involving an (eruptive) luminous blue variable event, e.g. within a blue loop (Chita et al. 2008; Mackey et al. 2012), however less in accordance with the dust size measures of Rubio et al. (2020) shown to be typical for red supergiants. Their constraint of the initial mass of WR136 to $\approx 50\text{--}60 M_\odot$ might reconcile both arguments, dust and asymmetries being generated at different phases of the complex evolution of a (potentially multiple) stellar system. Our allegation that the driving stellar object of NGC 6888 is not, despite the findings of Stock & Barlow (2014); Rubio et al. (2020), a single star, is supported by the detection of periodical modulation in line emission from the Wolf-Rayet star WR 134, interpretable as an inhomogeneous outflow (Morel et al. 1998) or as a trace of a so far undetected close companion (Meyer et al. 2018). The close companions to evolved massive stars Koenigsberger & Schmutz (2020) and the circumstellar nebulae of extragalactic Wolf-Rayet stars such as GR290 in the Galaxy M33 (Maryeva et al. 2018, 2020) also support our arguments. All this motivates further investigations of that problem.

5 CONCLUSION

In this paper we study the possibility of forming asymmetric Wolf-Rayet nebulae as a direct result of equatorial anisotropies in the blue supergiant stellar wind preceding the Wolf-Rayet phase. We present a two-winds toy model for the investigation of circumstellar medium generated from the evolutionary phase transition of different latitude-dependent distributions. Our MHD simulations are performed with a spherically-symmetric grid in the 2.5D fashion, using the PLUTO code (Mignone et al. 2007, 2012; Vaidya et al. 2018). We concentrate on the ~ 10 pc surrounding the star, and treat both stellar magnetic field and stellar rotation, using a combination of the recipe for asymmetric winds of Raga et al. (2008) and magnetised astrospheres (Parker 1958). This study updates the pioneering work of Brighenti & D’Ercole (1997) on the early aspherical evolution of young Wolf-Rayet nebulae from red supergiant stars. Particularly, our toy model permits to change the rotation, mass-loss, magnetic properties of the evolving stars, while simultaneously exploring the phase transition interval between the two evolutionary stages. It allows us to explore at reduced computational costs, the wind-wind interaction of typical magnetised stellar outflows responsible for the shaping of circumstellar nebulae. We also explore, by means of radiative transfer calculations, the emission properties of those gas nebulae.

The density distribution in the pre-Wolf-Rayet surroundings is directly responsible for the shaping of our Wolf-Rayet nebulae and the stellar magnetic field seems to be dynamically unimpor-

tant in the process of producing the bipolarities, in the sense that only evolving MHD flows in rotation produce spherical nebulae, at least in the corner of the parameter space of blue supergiant and subsequent Wolf-Rayet stars that we explore. An equatorially compressed circumstellar distribution gives the Wolf-Rayet stellar wind a peanut-like morphology, which is further elongated along the polar direction as a jet-like shape if the polar-to-equatorial density distribution ratio increases, or in case a substantially long phase transition period (\sim kyr) between the two winds. The topology of the magnetic field lines is greatly modified when the Wolf-Rayet wind starts blowing into the previous cold material. The rotating blue supergiant dipole B_ϕ sees its magnetic field lines opened and channelled to the poles of the structure. Interestingly, all our nebulae are shaped by wind-wind interaction taking place in the free-streaming stellar wind of the ancestor star, i.e. inside of the termination shock of its main-sequence stellar wind bubble (Weaver et al. 1977). This implies that the nebulae will appear the same regardless of their driving star's bulk motion (Meyer et al. 2020) and that the nebulae are free of ISM material. We propose to characterise the evolution of MHD asymmetric Wolf-Rayet nebulae in the ρ - v - B_ϕ diagram, which we show to concisely report the main feature of our MHD Wolf-Rayet nebulae as a characteristic S-shape.

Radiative transfer calculations against dust opacity of the Wolf-Rayet nebulae provided us with mid-infrared $24\ \mu\text{m}$ synthetic emission maps, showing that their projected emission reflects the anisotropies of the blue pre-Wolf-Rayet wind. We demonstrate that projection effects play a non-negligible role in the shaping of observed Wolf-Rayet nebulae. According to the observer's viewing angle, these transient objects can appear as an oblate form, a bipolar structure, an ellipse or a ring. Last, we discuss the potential origins of the pre-Wolf-Rayet circumstellar anisotropies. Two main scenarios have been identified so far, involving either a red or a blue supergiant star. However, we show that solely the blue supergiant one can, within the single star scenario, generate density distributions sufficiently asymmetric to channel the Wolf-Rayet stellar wind and to produce Wolf-Rayet nebulae's bipolarity. This lead us to question the well-accepted past evolution of the famous asymmetric bubble nebula NGC 6888 around the Wolf-Rayet WR 136, believed to be the archetypal resulting nebulae of a single red supergiant-to-Wolf-Rayet-evolving star. We propose that NGC 6888 might be driven by a multiple system, or underwent additional evolutionary phases.

ACKNOWLEDGEMENTS

The author thanks the referee A. Raga from the University of Mexico for his numerous comments which greatly improved the quality of the paper. The author thanks L. Oskinova from the University of Potsdam for discussions regarding evolved massive stars. The author acknowledges the North-German Supercomputing Alliance (HLRN) for providing HPC resources that have contributed to the research results reported in this paper.

DATA AVAILABILITY

This research made use of the PLUTO code developed at the University of Torino by A. Mignone and collaborators (<http://plutocode.ph.unito.it/>) and of the RADMC-3D code developed by C. Dullemond and collaborators at the University of Heidelberg (<https://www.ita.uni-heidelberg.de/>

[~dullemond/software/radmc-3d/](https://www.ita.uni-heidelberg.de/~dullemond/software/radmc-3d/)), respectively. The figures have been produced using the Matplotlib plotting library for the Python programming language (<https://matplotlib.org/>). The data underlying this article will be shared on reasonable request to the corresponding author.

REFERENCES

- Bestenlehner J. M., Gräfener G., Vink J. S. e. a., 2014, *A&A*, 570, A38
 Bjorkman J. E., Wood K., 2001, *ApJ*, 554, 615
 Blondin J. M., Lundqvist P., Chevalier R. A., 1996, *ApJ*, 472, 257
 Brighenti F., D'Ercole A., 1997, *MNRAS*, 285, 387
 Brott I., de Mink S. E., Cantiello M., Langer N., de Koter A., Evans C. J., Hunter I., Trundle C., Vink J. S., 2011, *A&A*, 530, A115
 Chevalier R. A., 1977, *ARA&A*, 15, 175
 Chevalier R. A., Liang E. P., 1989, *ApJ*, 344, 332
 Chevalier R. A., Luo D., 1994, *ApJ*, 421, 225
 Chita S. M., Langer N., van Marle A. J., García-Segura G., Heger A., 2008, *A&A*, 488, L37
 Chu Y. H., 1981, *ApJ*, 249, 195
 Chu Y. H., 1982a, *ApJ*, 254, 578
 Chu Y. H., 1982b, *ApJ*, 255, 79
 Chu Y. H., 1983, *ApJ*, 269, 202
 Chu Y. H., Treffers R. R., 1981, *ApJ*, 250, 615
 Chu Y. H., Treffers R. R., Kwitter K. B., 1983, *ApJS*, 53, 937
 Ciotti L., D'Ercole A., 1989, *A&A*, 215, 347
 Comerón F., Kaper L., 1998, *A&A*, 338, 273
 Crowther P. A., 2007, *ARA&A*, 45, 177
 Decin L., 2020, arXiv e-prints
 Decin L., Montargès M., Richards A. M. S., Gottlieb C. A., Homan W., McDonald I. e. a., 2020, *Science*, 369, 1497
 Dopita M. A., Bell J. F., Chu Y. H., Lozinskaya T. A., 1994, *ApJS*, 93, 455
 Dullemond C. P., 2012, RADMC-3D: A multi-purpose radiative transfer tool, *Astrophysics Source Code Library*
 Dwarkadas V. V., 2005, *ApJ*, 630, 892
 Dwarkadas V. V., 2007, *ApJ*, 667, 226
 Ekström S., Georgy C., Eggenberger P., Meynet G., Mowlavi N., Wyttenbach A., Granada A., Decressin T., Hirschi R., Frischknecht U., Charbonnel C., Maeder A., 2012, *A&A*, 537, A146
 Esteban C., Mesa-Delgado A., Morisset C., García-Rojas J., 2016, *MNRAS*, 460, 4038
 Faherty J. K., Shara M. M., Zurek D., Kanarek G., Moffat A. F. J., 2014, *AJ*, 147, 115
 Fang J., Yu H., Zhang L., 2017, *MNRAS*, 464, 940
 Fernández-Martín A., Martín-Gordón D., Vílchez J. M., Pérez Montero E., Riera A., Sánchez S. F., 2012, *A&A*, 541, A119
 Flagey N., Noriega-Crespo A., Petric A., Geballe T. R., 2014, *AJ*, 148, 34
 Frank A., Balick B., Davidson K., 1995, *ApJ*, 441, L77
 Freyer T., Hensler G., Yorke H. W., 2003, *ApJ*, 594, 888
 Freyer T., Hensler G., Yorke H. W., 2006, *ApJ*, 638, 262
 Gabler M., Wongwathanarat A., Janka H.-T., 2021, *MNRAS*, 502, 3264
 García-Segura G., Langer N., Mac Low M.-M., 1996, *A&A*, 316, 133
 García-Segura G., Langer N., Różyczka M., Franco J., 1999, *ApJ*, 517, 767
 García-Segura G., Mac Low M.-M., Langer N., 1996, *A&A*, 305, 229
 García-Segura G., Ricker P. M., Taam R. E., 2018, *ApJ*, 860, 19
 García-Segura G., Taam R. E., Ricker P. M., 2020, *ApJ*, 893, 150
 González R. F., de Gouveia Dal Pino E. M., Raga A. C., Velázquez P. F., 2004, *ApJ*, 616, 976
 Groh J. H., Meynet G., Ekström S., Georgy C., 2014, *A&A*, 564, A30
 Guerrero M. A., Chu Y.-H., 2008, *ApJS*, 177, 216
 Gvaramadze V. V., Kniazev A. Y., Fabrika S., 2010, *MNRAS*, 405, 1047
 Gvaramadze V. V., Kniazev A. Y., Maryeva O. V., Berdnikov L. N., 2018, *MNRAS*, 474, 1412
 Hamann W. R., Gräfener G., Liermann A., 2006, *A&A*, 457, 1015
 Harten A., Lax P. D., van Leer B., 1983, *SIAM Review*, 25, 35

- Heiligman G. M., 1980, *MNRAS*, 191, 761
- Herbst K., Scherer K., Ferreira S. E. S., Baalman L. R., Engelbrecht N. E., Fichtner H., Kleimann J., Strauss R. D. T., Moeketsi D. M., Mohamed S., 2020, *ApJ*, 897, L27
- Hirai R., Podsiadlowski P., Owocki S. P., Schneider F. R. N., Smith N., 2021, *MNRAS*, 503, 4276
- Hung C. S., Ou P.-S., Chu Y.-H., Gruendl R. A., Li C.-J., 2021, *ApJS*, 252, 21
- Kervella P., Decin L., Richards A. M. S., Harper G. M., McDonald I., O’Gorman E., Montargès M., Homan W., Ohnaka K., 2018, *A&A*, 609, A67
- Koenigsberger G., Schmutz W., 2020, *A&A*, 639, A18
- Langer N., 2012, *ARA&A*, 50, 107
- Langer N., García-Segura G., Mac Low M.-M., 1999, *ApJ*, 520, L49
- Laor A., Draine B. T., 1993, *ApJ*, 402, 441
- Mackey J., Mohamed S., Gvaramadze V. V., Kotak R., Langer N., Meyer D. M.-A., Moriya T. J., Neilson H. R., 2014, *Nature*, 512, 282
- Mackey J., Mohamed S., Neilson H. R., Langer N., Meyer D. M.-A., 2012, *ApJ*, 751, L10
- Maeder A., 2009, *Physics, Formation and Evolution of Rotating Stars*, springer-verlag edn. *Astronomy and Astrophysics Library*
- Mahy L., Hutsemékers D., Royer P., Waelkens C., 2016, *A&A*, 594, A94
- Marchenko S. V., Moffat A. F. J., Crowther P. A., 2010, *ApJ*, 724, L90
- Marston A. P., Chu Y. H., Garcia-Segura G., 1994, *ApJS*, 93, 229
- Marston A. P., Yocum D. R., Garcia-Segura G., Chu Y. H., 1994, *ApJS*, 95, 151
- Maryeva O., Koenigsberger G., Egorov O., Rossi C., Polcaro V. F., Calabresi M., Viotti R. F., 2018, *A&A*, 617, A51
- Maryeva O. V., Koenigsberger G., Karpov S. V., Lozinskaya T. A., Egorov O. V., Rossi C., Calabresi M., Viotti R. F., 2020, *A&A*, 635, A201
- Mesa-Delgado A., Esteban C., García-Rojas J., Reyes-Pérez J., Morisset C., Bresolin F., 2014, *ApJ*, 785, 100
- Meyer D. M.-A., Kuiper R., Kley W., Johnston K. G., Vorobyov E., 2018, *MNRAS*, 473, 3615
- Meyer D. M. A., Mignone A., Petrov M., Scherer K., Velazquez P. F., Boumis P., 2021, arXiv e-prints, p. arXiv:2107.05513
- Meyer D. M. A., Oskinova L. M., Pohl M., Petrov M., 2020, *MNRAS*, 496, 3906
- Meyer D. M. A., Petrov M., Pohl M., 2020, *MNRAS*, 493, 3548
- Meyer D. M. A., Pohl M., Petrov M., Oskinova L., 2021, *MNRAS*, 502, 5340
- Mignone A., Bodo G., Massaglia S., Matsakos T., Tesileanu O., Zanni C., Ferrari A., 2007, *ApJS*, 170, 228
- Mignone A., Zanni C., Tzeferacos P., van Straalen B., Colella P., Bodo G., 2012, *ApJS*, 198, 7
- Moens N., Sundqvist J. O., El Mellah I., Poniatowski L., Teunissen J., Keppens R., 2021, arXiv e-prints, p. arXiv:2104.03968
- Morel T., Marchenko S. V., Eenens P. R. J., Moffat A. F. J., Koenigsberger G., Antokhin I. I., Eversberg T., Tovmassian G. H., Hill G. M., Cardona O., St-Louis N., 1998, *Ap&SS*, 260, 173
- Müller B., Janka H. T., 2015, *MNRAS*, 448, 2141
- Parker E. N., 1958, *ApJ*, 128, 664
- Parker R. A. R., 1978, *ApJ*, 224, 873
- Pogorelov N. V., Matsuda T., 2000, *A&A*, 354, 697
- Pogorelov N. V., Semenov A. Y., 1997, *A&A*, 321, 330
- Pogorelov N. V., Zank G. P., Ogino T., 2004, *ApJ*, 614, 1007
- Powell K. G., 1997, *An Approximate Riemann Solver for Magnetohydrodynamics*. Springer Berlin Heidelberg, Berlin, Heidelberg, pp 570–583
- Prajapati P., Tej A., del Palacio S., Benaglia P., CH I.-C., Vig S., Mandal S., Kanti Ghosh S., 2019, *ApJ*, 884, L49
- Raga A. C., Cantó J., De Colle F., Esquivel A., Kajdic P., Rodríguez-González A., Velázquez P. F., 2008, *ApJ*, 680, L45
- Rozyczka M., Franco J., 1996, *ApJ*, 469, L127
- Rubio G., Toalá J. A., Jiménez-Hernández P., Ramos-Larios G., Guerrero M. A., Gómez-González V. M. A., Santamaría E., Quino-Mendoza J. A., 2020, *MNRAS*, 499, 415
- Sander A., Hamann W. R., Todt H., 2012, *A&A*, 540, A144
- Scherer K., Baalman L. R., Fichtner H., Kleimann J., Bomans D. J., Weis K., Ferreira S. E. S., Herbst K., 2020, *MNRAS*, 493, 4172
- Smartt S. J., 2009, *ARA&A*, 47, 63
- Smartt S. J., Lennon D. J., Kudritzki R. P., Rosales F., Ryans R. S. I., Wright N., 2002, *A&A*, 391, 979
- Smith N., 2017, *Philosophical Transactions of the Royal Society of London Series A*, 375, 20160268
- Stock D. J., Barlow M. J., 2014, *MNRAS*, 441, 3065
- Szécsi D., Wünsch R., Agrawal P., Langer N., 2020, arXiv e-prints, p. arXiv:2004.08203
- Toalá J. A., Arthur S. J., 2011, *ApJ*, 737, 100
- Toalá J. A., Guerrero M. A., Chu Y. H., Gruendl R. A., Arthur S. J., Smith R. C., Snowden S. L., 2012, *ApJ*, 755, 77
- Toalá J. A., Guerrero M. A., Gruendl R. A., Chu Y. H., 2014, *AJ*, 147, 30
- Toalá J. A., Guerrero M. A., Ramos-Larios G., Guzmán V., 2015, *A&A*, 578, A66
- Toalá J. A., Oskinova L. M., Hamann W. R., Ignace R. e. a., 2018, *ApJ*, 869, L11
- Treffers R. R., Chu Y. H., 1982, *ApJ*, 254, 569
- Vaidya B., Mignone A., Bodo G., Rossi P., Massaglia S., 2018, *ApJ*, 865, 144
- van der Sluys M. V., Lamers H. J. G. L. M., 2003, *A&A*, 398, 181
- van Marle A. J., Keppens R., Meliani Z., 2011, *Bulletin de la Societe Royale des Sciences de Liege*, 80, 310
- van Marle A. J., Langer N., Achterberg A., García-Segura G., 2006, *A&A*, 460, 105
- van Marle A. J., Langer N., García-Segura G., 2005, *A&A*, 444, 837
- van Marle A. J., Langer N., García-Segura G., 2007, *A&A*, 469, 941
- van Marle A. J., Meliani Z., Keppens R., Decin L., 2011, *ApJ*, 734, L26
- van Marle A. J., Meliani Z., Marcowith A., 2015, *A&A*, 584, A49
- Vink J. S., 2006, in Lamers H. J. G. L. M., Langer N., Nugis T., Annuk K., eds, *Stellar Evolution at Low Metallicity: Mass Loss, Explosions, Cosmology Vol. 353 of Astronomical Society of the Pacific Conference Series, Massive star feedback – from the first stars to the present*. p. 113
- Vlemmings W. H. T., Diamond P. J., van Langevelde H. J., 2002, *A&A*, 394, 589
- Vlemmings W. H. T., van Langevelde H. J., Diamond P. J., 2005, *A&A*, 434, 1029
- Weaver R., McCray R., Castor J., Shapiro P., Moore R., 1977, *ApJ*, 218, 377
- Weiler K. W., Sramek R. A., 1988, *ARA&A*, 26, 295
- Weis K., Chu Y. H., Duschl W. J., Bomans D. J., 1997, *A&A*, 325, 1157
- Woosley S. E., Bloom J. S., 2006, *ARA&A*, 44, 507
- Woosley S. E., Heger A., Weaver T. A., 2002, *Reviews of Modern Physics*, 74, 1015
- Wrigge M., Chu Y.-H., Magnier E. A., Wendker H. J., 2005, *ApJ*, 633, 248